

**ספריות הטכניון**  
*The Technion Libraries*

**בית הספר ללימודים מוסמכים ע"ש ארוין וג'ואן ג'ייקובס**  
*Irwin and Joan Jacobs Graduate School*

©  
**All rights reserved to the author**

*This work, in whole or in part, may not be copied (in any media), printed, translated, stored in a retrieval system, transmitted via the internet or other electronic means, except for "fair use" of brief quotations for academic instruction, criticism, or research purposes only. Commercial use of this material is completely prohibited.*

©  
**כל הזכויות שמורות למחבר/ת**

אין להעתיק (במדיה כלשהי), להדפיס, לתרגם, לאחסן במאגר מידע, להפיצו באינטרנט, חיבור זה או כל חלק ממנו, למעט "שימוש הוגן" בקטעים קצרים מן החיבור למטרות לימוד, הוראה, ביקורת או מחקר. שימוש מסחרי בחומר הכלול בחיבור זה אסור בהחלט.

# **Integer-Only Cross Field Computation**

**Nahum Farchi**



# **Integer-Only Cross Field Computation**

Research Thesis

Submitted in partial fulfillment of the requirements  
for the degree of Master of Science in Computer Science

**Nahum Farchi**

Submitted to the Senate  
of the Technion — Israel Institute of Technology  
Sivan 5778      Haifa      May 2018



This research was carried out under the supervision of Prof. Mirela Ben-Chen, in the Faculty of Computer Science.

Some results in this thesis have been published as articles by the author and research collaborators in conferences and journals during the course of the author's master research period, the most up-to-date versions of which being:

Nahum Farchi and Mirela Ben-Chen. Integer-only cross field computation. *ACM Transactions on Graphics (TOG)*, 37(4), 2018.

## Acknowledgements

I would like to thank Mirela for patiently and thoughtfully guiding me throughout the process of writing this thesis. I also thank my family and friends for their endless encouragement and support.

The generous financial help of the Technion is gratefully acknowledged.



# Contents

## List of Figures

<b>Abstract</b>	<b>1</b>
<b>1 Introduction</b>	<b>3</b>
1.1 Related Work . . . . .	3
1.2 Contributions . . . . .	6
<b>2 Background: Angle-Based Cross Field Computation</b>	<b>7</b>
2.1 Notation . . . . .	7
2.2 MIQ: Mixed Integer Quadrangulation . . . . .	8
2.3 TC: Trivial Connections . . . . .	8
<b>3 Integer-Only Cross Field Computation</b>	<b>11</b>
3.1 TCO: Trivial Connections with Optimal Holonomies . . . . .	11
3.2 IOQ . . . . .	13
3.3 IOQr: Relaxation . . . . .	14
<b>4 Optimization</b>	<b>17</b>
4.1 Solving for $\alpha$ . . . . .	17
4.2 Solving for $\beta$ . . . . .	17
4.3 Initialization . . . . .	18
4.4 Convergence. . . . .	19
4.5 Parallelization . . . . .	19
<b>5 Approximation</b>	<b>23</b>
5.1 Background: The Resistance Distance . . . . .	23
5.2 Random Approximation . . . . .	23
<b>6 Implementation</b>	<b>29</b>
6.1 Limitations . . . . .	29
6.2 Results . . . . .	30
6.2.1 Comparisons . . . . .	30
6.2.2 Scalability . . . . .	32

6.2.3	Varying $\epsilon$ . . . . .	32
6.2.4	Stability to Noise . . . . .	33
6.2.5	Application to Quadrangulation . . . . .	33
<b>7</b>	<b>Conclusion</b>	<b>37</b>
<b>A</b>	<b>Appendix - Proofs.</b>	<b>39</b>
<b>B</b>	<b>Appendix - Supplementary Material.</b>	<b>43</b>
	<b>Hebrew Abstract</b>	<b>i</b>

# List of Figures

1.1 Our iterative optimization (bottom) finds a solution with lower energy, and fewer singularities than MIQ (top). . . . .	4
3.1 Computing the angle defects for (green) trivial and (blue) non-trivial cycles. For trivial cycles, we take $2\pi$ minus the sum of angles, which is the usual discrete Gaussian curvature. For non-trivial cycles, we take the sum of exterior angles along the blue curve—adding $\theta$ whenever the curve turns left, and subtracting $\theta$ whenever the curve turns right. . . . .	12
4.1 Comparison between direct rounding and an exact CVP solver [AEVZ02] for some low resolution meshes sorted by genus. Note that in most cases direct rounding yielded an optimal solution. Notable exceptions are the ball and heptoroid meshes, of genus 5 and 22 respectively, where CVP did improve the solution considerably. We also show the resulting cross fields for the ball mesh with $\beta$ computed by rounding (left) and CVP (right). . . . .	18
4.2 Final energy value (left) and final number of cone singularities (right) as we increase the number of initial singularities. We also show the energy value and number of singularities of MIQ [BZK09]. Note that our method is stable to the initialization, and in all cases yields a better energy than MIQ with fewer singularities. . . . .	19
4.3 The average of $\alpha$ across $N$ random initializations for the initial (a) and final (b) iterations. Note that the singularities concentrate at specific locations, yet there might be multiple equivalent configurations, e.g. on the tail. We also show one of our results (c) and the MIQ result (d). . . . .	20
5.1 The results of our exact and approximated algorithms (IOQ and IOQe), compared with MIQ [BZK09] and GO [KCPS13], on two symmetric models. See the text for details. . . . .	24
5.2 Left: Energy values during the iterations for different numbers of initial singularities, for both the exact (IOQ) and approximated (IOQe) methods. Right: Close-up of the same graph. Note that the energy plot of the approximated method is nearly indistinguishable from the exact method.	25

5.3	Left: Histogram of the pair-wise distortions $R_{ij}/(\tilde{R}_\epsilon)_{ij}$ for three values of $\epsilon$ . Right: Percentage of pairs with distortion greater than 10% as we increase the projected dimension $k$ . See the text for details. . . . .	26
5.4	The resistance distance and its approximations as we increase $\epsilon$ , with respect to the red point. Here we show the running time in seconds, $T$ , and the original and projected dimension, $n$ and $k$ respectively. . . . .	26
5.5	Time/quality tradeoff of IOQ $\epsilon$ with different $\epsilon$ values. We show the average across $N = 300$ experiments of $\alpha$ after convergence, using (a) the exact resistance distance with different initial random $\alpha$ ; and (b-d) the approximate resistance, with different random projections and the same initial $\alpha$ . Note that for $\epsilon = 0.5$ we get a dimensionality reduction of more than 90%, yet the algorithm yields excellent cone positions. . . . .	27
6.1	An example of our method with the graph Laplacian (left) and the cotangent Laplacian (middle) compared to MIQ (right). Note that in both cases our method finds a better solution in terms of smoothness energy and singularity placement. . . . .	30
6.2	The improvement in energy and singularities of our exact (IOQ) and approximate (IOQe) methods relative to MIQ, computed by $(E_{MIQ}/E_{ours})(( S _{MIQ} + 1)/( S _{ours} + 1))$ on the meshes from [MPZ14], where $ S $ is the number of singularities. Note that for all meshes our result is bigger than 1, and thus improves on MIQ. Furthermore, the results of IOQ and IOQe are comparable for most meshes. . . . .	31
6.3	The improvement in energy and singularities of our exact (IOQ) and approximate (IOQe) methods relative to GO [KCPS13], using the same protocol as in Figure 6.2. Here, again, for all meshes our result is bigger than 1, and thus improves on GO. Furthermore, the results of IOQ and IOQe are comparable for most meshes. . . . .	32
6.4	Some meshes from the benchmark and their cross fields. Note that our method yields considerably fewer singularities with lower energy values. . . . .	34
6.5	Energy, number of singularities and timing scalability, on a series of meshes with varying resolutions. See the text for details. . . . .	35
6.6	Varying the approximation parameter, $\epsilon$ , has little effect on the final singularity placement. Note in particular that even with a projected dimension of $k = 213$ , our method still places most of the singularities on the corners as desired, albeit with a somewhat higher energy. . . . .	35
6.7	Stability of our method (left) compared to MIQ (right) with increasing levels of normal noise added to the vertex positions. . . . .	35

6.8	The results of our method (left) compared to MIQ (right) on a uniform and non-uniform triangulation. Note that while our method does not incorporate the geometry in the system matrix $L$ , it is, at least to some extent, robust to changes in the triangulation. . . . .	36
6.9	Quadrangular meshes generated from our cross fields (left,center), compared to quad meshes generated from MIQ cross fields (right). . . . .	36
B.1	Number of singularities. . . . .	43
B.2	Energy. . . . .	44
B.3	Timing in seconds. . . . .	44



# Abstract

Directional fields are important objects in geometry processing with applications ranging from texture synthesis to non-photorealistic rendering, quadrangular remeshing, and architectural design. In this thesis, we focus our attention on cross fields – a direction field in which four unit vectors with  $\pi/2$  symmetry are defined at each point on the surface.

Computing smooth cross fields on triangle meshes is challenging, as the problem formulation inherently depends on *integer* variables to encode the invariance of the crosses to rotations by integer multiples of  $\pi/2$ . Furthermore, finding the optimal placement for the cone singularities is essentially a hard combinatorial problem.

We propose a new iterative algorithm for computing smooth cross fields on triangle meshes that is simple, easily parallelizable on the GPU, and finds solutions with lower energy and fewer cone singularities than state-of-the-art methods. Furthermore, the output cross fields are such that there is no relocation of a single  $\pm\pi/2$  singularity that will reduce the energy.

Our approach is based on a formal equivalence, which we prove, between two formulations of the optimization problem. This equivalence allows us to eliminate the real variables and design an efficient grid search algorithm for the cone singularities. We leverage a recent graph-theoretical approximation of the *resistance distance matrix* of the triangle mesh to speed up the computation and enable a trade-off between the computation time and the smoothness of the output.



# Chapter 1

## Introduction

Directional fields, and especially *cross fields*, are important objects in geometry processing. They are used in many applications, from quadrangular remeshing to non-photorealistic rendering [VCD<sup>+</sup>16]. Computing smooth cross fields on triangle meshes is challenging, as the problem formulation inherently depends on *integer* variables to encode the invariance of the crosses to rotations by integer multiples of  $\pi/2$ .

A popular approach, suggested by Bommes et al. [2009], formulates a mixed-integer optimization problem and solves it greedily to compute the cross field. While highly efficient and effective, the greedy solution can lead to sub-optimal results, as in Fig. 1.1 (top). Alternatively, Crane et al. [2010] (TCODS) [CDS10] posed the problem in terms of *angle defects* due to parallel transport on closed cycles, leading to a sparse linear least squares problem that is solved efficiently when the defects are known.

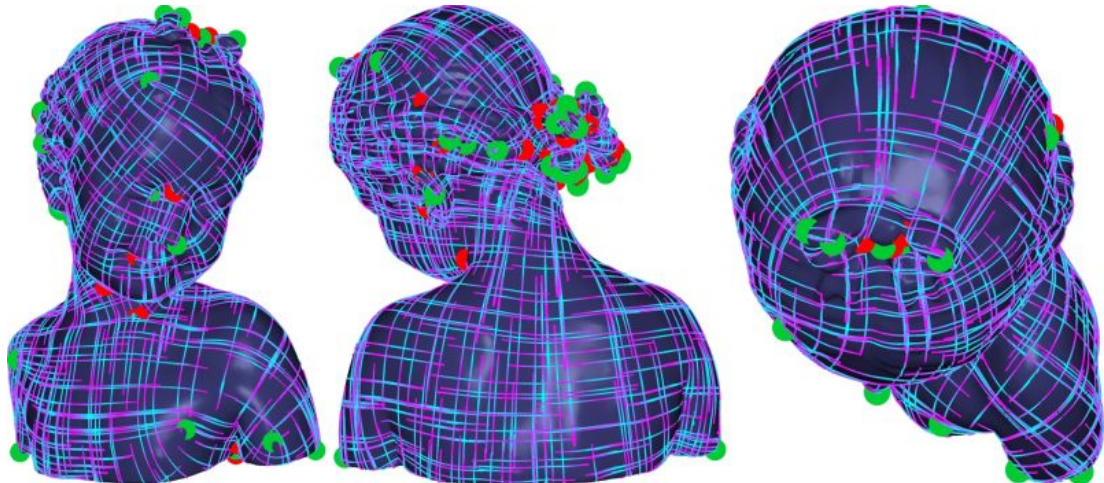
We show that if the angle defects are *unknown*, and there are no directional constraints, these two optimization problems are *equivalent*. Furthermore, by eliminating the real variables, we remain with an *integer only* optimization problem. We use this insight to design a new iterative algorithm for minimizing the energy that is simple, easily parallelizable on the GPU, and finds solutions with lower energy and fewer singularities than MIQ, e.g. Fig. 1.1 (bottom). Finally, we show the connection of the minimized energy to the *resistance distance matrix* of the triangle mesh, and leverage a recent graph theoretical approximation to speed up the computation and allow us to trade-off the computation time and the quality of the resulting cross field.

### 1.1 Related Work

Cross field computation, and directional field computation in general, has seen a surge of research in recent years. A recent review [VCD<sup>+</sup>16] covers the latest developments, and we therefore focus our literature review on methods closest to our approach.

**Angle based representation.** A popular formulation of the cross field computation problem is to represent every cross as an *angle* with respect to a fixed local orthogonal

MIQ,  $E = 82.46, |S| = 86$



IOQe  $\epsilon = .5, E = 59.10, |S| = 28$

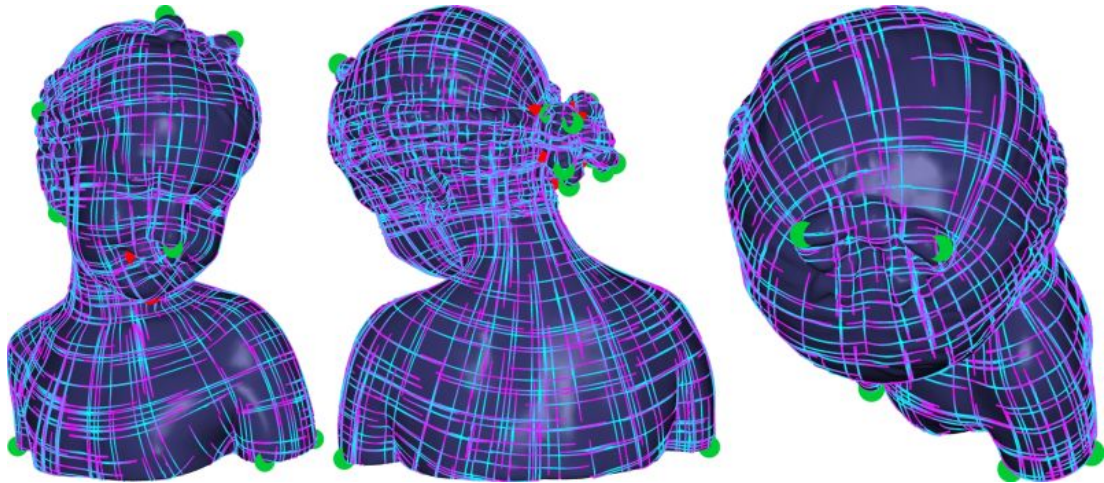


Figure 1.1: Our iterative optimization (bottom) finds a solution with lower energy, and fewer singularities than MIQ (top).

frame. Since crosses are invariant to rotations by integer multiples of  $\pi/2$ , such a representation has an inherent phase ambiguity. Therefore, finding a *smooth* assignment of crosses inevitably requires taking into account these unknown integer phases, leading to optimization problems with integer variables. Bommes et al. [2009] suggested one of the first efficient methods to tackle these optimization problems in the context of cross field generation, by greedily rounding to an integer one variable per iteration and resolving the system. Our approach optimizes the same energy greedily, albeit using a different algorithm that guarantees that there exists no modification of a single  $\pm\frac{\pi}{2}$  singularity’s position that reduces the energy. This leads to lower energy values and better singularity placement. A different angle based approach, suggested by Crane et al. [2010], encodes the *angle difference* per edge instead of an angle per face. This representation leads to a minimum norm linear least squares optimization problem with constraints, where the integer variables now arise as the constrained values. Furthermore, Crane et al. [2013, Sec. 8.4.1] have shown that it is possible to solve this optimization problem by solving a single Poisson problem when the integer variables are known. We use this formulation with *unknown* angle defect values as the basis for our algorithm.

**Cartesian representation.** An alternative to the angle based representation is to represent the direction as two coordinate values with respect to a local frame [RLL<sup>+</sup>06] or, equivalently, as a complex number [KCPS13]. The explicit encoding of the integer phase is not required in this representation, albeit, depending on the choice of smoothness energy, a non-convex pointwise unit-length constraint might be required. Without the unit-length constraint, this formulation leads to an unconstrained linear least squares problem that can be efficiently and globally solved [KCPS13]. Our main interest is in the angle-based energy, as it has various advantages in applications; see [VCD<sup>+</sup>16]. We show that for this energy our algorithm achieves lower energy values, with a smaller number of singularities, compared to competing approaches.

**Scalable cross field computation.** Recently, new methods have been proposed [JTPSH15] for efficient cross field computation that are applicable to meshes with millions of triangles. Such approaches often work locally, leading to a very efficient solution at the price of cross field quality in terms of the number of singularities and field smoothness. Our approach is at the other end of the spectrum, namely, we invest more computational time and generate a higher quality cross field. We further allow a trade-off between computational time and cross field quality using a single parameter. Finally, our time/quality trade-off is implemented using a simple algebraic approach with random projections, and does not require constructing multi-resolution hierarchies of the input shape.

**Parameterization with cone singularities.** Cross field computation is closely related to mesh parameterization. Specifically, one of the main applications of cross fields is quadrangular remeshing, where the parameterization gradients are aligned to the

cross directions. Then, the singularities of the cross field become the non-regular vertices of the quad mesh. Hence, it is in general beneficial to generate smooth cross fields with a small number of singularities. As an alternative to generating a cross field and using it for creating a parameterization, it is possible to compute a parameterization with *cone singularities* given a *holonomy signature*. Such conformal parameterizations were suggested [BCGB08, SSP08], as well as variants that use other energies [MZ12, MZ13], guarantee bijectivity [BCW17] or generate a seamless similarity map that can be used for constructing  $C^2$  surfaces [CZ17b]. While our approach generates cross fields, it is based on finding a holonomy signature, and thus can be used to generate inputs for cone parameterization methods such as [BCW17, CZ17b].

**Connectivity Editing.** Peng et al. [2001] have proposed a set of edit operations on a convex region of the quadrangular mesh to improve the placement of irregular vertices (i.e., vertices with valence different than four). For example, they show that the global placement of a single irregular vertex is in some sense rigid, whereas singularity pairs in close proximity can be locally moved to improve the structure of the quadrangular mesh. In contrast, our approach guarantees that no movement of a single singularity, or the global cancellation of a  $\pm\pi/2$  singularity pair can improve the energy. It would be interesting to explore their other suggested edit operations to locally improve the quadrangular mesh structure after generating the global structure using our method.

## 1.2 Contributions

We show the equivalence between computing smooth cross fields and finding optimal holonomy signatures in the absence of directional constraints, and leverage it to design a novel algorithm that optimizes the angle-based cross field smoothness energy. Our approach has the following advantages:

- The algorithm is simple, easily parallelizable and finds cross fields with lower energy values than existing approaches.
- The output cross fields are such that there is no relocation of a single  $\pm\frac{\pi}{2}$  singularity that will reduce the energy. This leads to cross fields with fewer singularities, and singularities that are better placed, compared to existing methods.
- The formulation is based on the resistance distance matrix, which has a well-known random approximation with theoretical guarantees. We use this approximation to trade-off between cross field smoothness and computation time.

## Chapter 2

# Background: Angle-Based Cross Field Computation

### 2.1 Notation

Let  $\mathcal{M} = (\mathcal{V}, \mathcal{E}, \mathcal{F})$  be a 2-manifold closed orientable triangle mesh, where  $\mathcal{V}$  are the vertices,  $\mathcal{E}$  are the edges and  $\mathcal{F}$  are the faces. We denote  $n = |\mathcal{V}|, l = |\mathcal{E}|, m = |\mathcal{F}|$ , the genus of  $\mathcal{M}$  by  $g$ , and its Euler characteristic by  $\chi = 2 - 2g$ . We further denote the *dual* mesh by  $\mathcal{M}^* = (\mathcal{V}^*, \mathcal{E}^*, \mathcal{F}^*) = (\mathcal{F}, \mathcal{E}^*, \mathcal{V})$ . Following existing work, see e.g. [VCD<sup>+</sup>16, Sec. 5.1], we represent crosses using angles. Thus, we use  $\theta \in \mathbb{R}^m$  to denote angles on the faces, which are measured relative to a local frame of reference, i.e., a pair of orthogonal unit vectors tangent to the face. We further assume that each edge in  $\mathcal{E}$  has a known, arbitrary orientation that also induces an orientation on the corresponding dual edge. We denote by  $r \in \mathbb{R}^l$  the *oriented* angle difference between the reference frames on adjacent faces. We slightly abuse notation by addressing elements of  $r$  both as  $r_e$  and as  $r_{ij}$  where  $e = (i, j) \in \mathcal{E}^*, i, j \in \mathcal{F}$ . Finally,  $d_0 \in \mathbb{Z}^{l \times n}$  and  $d_1 \in \mathbb{Z}^{m \times l}$  denote the edge-vertex and face-edge adjacency matrices, respectively, also known as the *discrete exterior derivatives* on 0- and 1-forms [CDGDS13].

A natural way to define the smoothness of an angle-based cross field is to consider the change in the angle between adjacent faces. Two methods that were suggested in the literature, MIQ [BZK09] and TC [CDS10], approach this problem using different formulations. In the following, we first present the two optimization problems as they were originally suggested. Then, in Section 3 we generalize TC, and show that the new formulation is equivalent to MIQ, yet simpler to optimize. We provide only a brief overview of the methods, and refer to specific sections of the survey [VCD<sup>+</sup>16] and course [CDGDS13] for basic concepts.

## 2.2 MIQ: Mixed Integer Quadrangulation

Bommes et al. [2009] represented a cross field by an angle per face,  $\theta \in \mathbb{R}^m$ , relative to a fixed local orthogonal frame. To account for the symmetry of the crosses with respect to rotations by  $\pi/2$ , additional *period jumps*,  $p \in \mathbb{Z}^l$ , were introduced. The MIQ objective function is given by:

$$E_M(\theta, p) = \sum_{(i,j) \in \mathcal{E}^*} (\theta_i + r_{ij} + \frac{\pi}{2} p_{ij} - \theta_j)^2. \quad (2.1)$$

We will assume a single directional constraint is given at a face  $c \in \mathcal{F}$ , with  $\theta_c = \theta_0$ . This objective function has multiple minimizers, which can be obtained by modifying  $\theta$  and  $p$  simultaneously. Therefore, to reduce the search space, Bommes et al. [2009] used a spanning tree  $\mathcal{T} \subset \mathcal{E}^*$  of the dual mesh  $\mathcal{M}^*$ , rooted at the constrained face  $c$ , and defined the optimization problem:

$$\begin{aligned} & \underset{\theta \in \mathbb{R}^m, p \in \mathbb{Z}^l}{\text{minimize}} && E_M(\theta, p) \\ & \text{subject to} && p_e = 0, \quad \forall e \in \mathcal{T}, \\ & && \theta_c = \theta_0. \end{aligned} \quad (2.2)$$

Effectively, the constraints can be easily eliminated, leading to an unconstrained mixed-integer problem in  $m-1$  real-valued variables and  $l-m+1=n+2g-1$  integer-valued variables.

## 2.3 TC: Trivial Connections

Alternatively, instead of solving for the angles on the faces, Crane et al. [2010] suggested to solve for the *adjustment angles*, or *connection* on the edges. As these define the *change* in the angle when passing on a dual edge [VCD<sup>+</sup>16, Sec.4.3], explicitly encoding the period jumps is not required. Hence, the real-valued variables  $x \in \mathbb{R}^l$  encode the change in angle, and the objective function is given by:

$$E_T(x) = \|x\|_2^2. \quad (2.3)$$

The angles  $\theta$  are obtained by integrating  $x$  along a dual tree  $\mathcal{T}$  rooted at the constrained face  $c$ , such that  $\theta_j = \theta_i + r_{ij} + x_{ij}$  for  $(i, j) \in \mathcal{T} \subset \mathcal{E}^*$ .

While this objective function does not depend on integer variables, not every  $x \in \mathbb{R}^l$  is valid, as different integration paths should yield the same angle up to rotation by  $\pi/2$ . Thus, additional constraints are required, leading to the optimization problem:

$$\begin{aligned}
& \underset{x \in \mathbb{R}^l}{\text{minimize}} && E_T(x) \\
& \text{subject to} && \Gamma x = \frac{\pi}{2}s - s_g(\Gamma).
\end{aligned} \tag{2.4}$$

Here,  $\Gamma \in \mathbb{Z}^{n+2g \times l}$  is a matrix whose rows form a spanning set of the dual cycles of  $\mathcal{M}$ . Specifically,  $\Gamma^T = [d_0, H]$ , where  $d_0 \in \mathbb{Z}^{l \times n}$  is the oriented edge-vertex incidence matrix, whose columns form a spanning set of the *contractible* dual cycles, and  $H \in \mathbb{Z}^{l \times 2g}$  is a matrix whose columns form a basis for the non-contractible dual cycles (see [CDGDS13, Sec. 8.2.2] for the construction of  $H$ ). Further,  $s_g(\Gamma) \in \mathbb{R}^{n+2g}$  contains the *angle defects* [VCD<sup>+</sup>16, Sec.6.2] around the basis cycles of  $\Gamma$ . The angle defects for the contractible cycles are given by the discrete Gaussian curvature of the vertices, and thus sum to  $2\pi\chi$  by the discrete Gauss-Bonnet formula [MDSB03].

Finally,  $s \in \mathbb{Z}^{n+2g}$  is a user prescribed integer *holonomy signature* that defines the number of integer rotations by  $\pi/2$  when parallel transporting a vector along the dual cycles in  $\Gamma$ . Since every column of  $d_0^T$  sums to 0, for the constraints to be feasible it is assumed that  $\sum_{i=1}^n s_i = 4\chi$ . Crane et al. [2010] showed that under this assumption the optimization problem (2.4) always has a solution, and a singularity of the cross field will arise at a vertex  $v_i \in \mathcal{V}, i \in \{1, \dots, n\}$  if and only if  $s_i \neq 0$ , i.e., the prescribed holonomy signature of the corresponding contractible dual cycle is non-zero.



## Chapter 3

# Integer-Only Cross Field Computation

### 3.1 TCO: Trivial Connections with Optimal Holonomies

A natural generalization of the TC approach is to add the integer holonomies as optimization variables instead of having the user prescribe them. This generalization leads to the optimization problem:

$$\begin{aligned} & \underset{x \in \mathbb{R}^l, \alpha \in \mathbb{Z}^n, \beta \in \mathbb{Z}^{2g}}{\text{minimize}} && E_T(x) \\ & \text{subject to} && \begin{bmatrix} d_0^T \\ H^T \end{bmatrix} x - \frac{\pi}{2} \begin{bmatrix} \alpha \\ \beta \end{bmatrix} = - \begin{bmatrix} \alpha_g \\ \beta_g(H) \end{bmatrix}, \\ & && \sum_{i=1}^n \alpha_i = 4\chi. \end{aligned} \quad (3.1)$$

Here, for notational convenience, we separate the holonomy signature as  $s = [\alpha, \beta]$ , where  $\alpha$  will denote the cone singularities vector and  $\beta$  the angle defects on non-contractible cycles. Similarly,  $\alpha_g$  is the discrete Gaussian curvature, and  $\beta_g(H)$  the geometric angle defects of the dual cycles in  $H$ , where both are computable from the geometry of the input mesh (see Figure 3.1).

A main result of this thesis is that the optimization problems in Equations (2.2) and (3.1) are equivalent. Formally, we have:

#### Theorem 3.1.

- (i) Let  $(\theta, p)$  be a feasible solution of (2.2). Then, for any integral basis of non-contractible dual cycles  $H$ , there exists a feasible solution  $(x, \alpha, \beta)$  of (3.1) such that  $E_T(x) = E_M(\theta, p)$ .
- (ii) Let  $(x, \alpha, \beta)$  be a feasible solution of (3.1). Then, for any dual spanning tree  $\mathcal{T}$ , there exists a feasible solution  $(\theta, p)$  of (2.2) such that  $E_M(\theta, p) = E_T(x)$ .

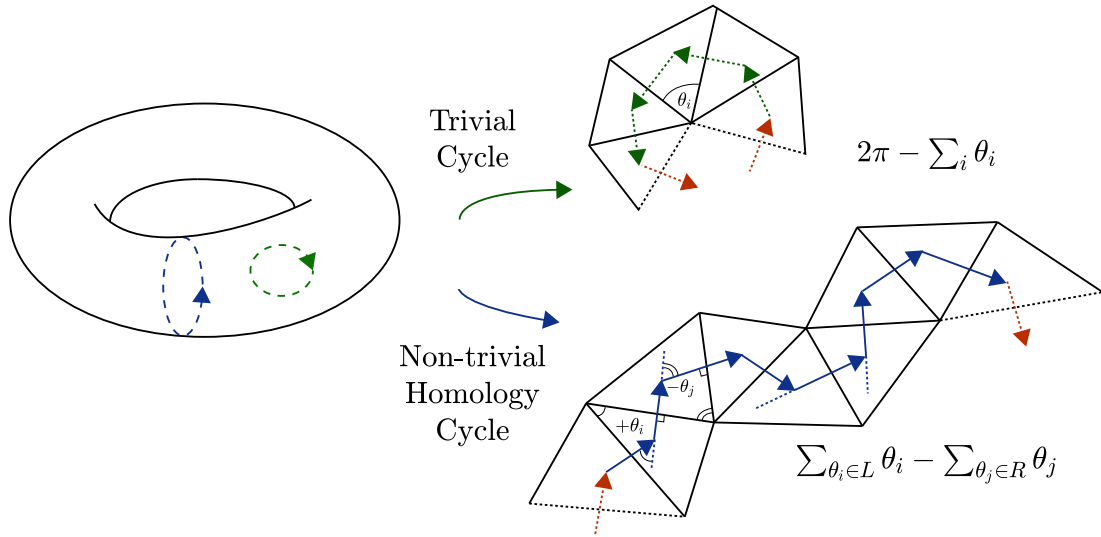


Figure 3.1: Computing the angle defects for (green) trivial and (blue) non-trivial cycles.

For trivial cycles, we take  $2\pi$  minus the sum of angles, which is the usual discrete Gaussian curvature. For non-trivial cycles, we take the sum of exterior angles along the blue curve—adding  $\theta$  whenever the curve turns left, and subtracting  $\theta$  whenever the curve turns right.

- (iii) Let  $(x, \alpha, \beta)$  and  $(\theta, p)$  be corresponding solutions as in (i,ii), and let  $\theta_T$  be the integrated values of  $x$ . Then  $\theta_T = \theta \bmod \pi/2$ .

A proof is given in the Appendix. The main building block of the proof is to relate the variables of the two optimization problems using a linear system of equations. We show that this system always has a unique solution that is integer-valued for  $p$  and  $(\alpha, \beta)$ . The integer solutions are guaranteed by a result from the theory of cycle bases on graphs [LR07], stating that a square submatrix of an integral cycle basis matrix, obtained by removing columns corresponding to edges of a spanning tree, is unimodular.

**Corollary 3.2.** *The optimization problems MIQ and TCO are invariant to the choice of dual spanning tree  $\mathcal{T}$  and basis for non-contractible cycles  $H$ , respectively. Specifically:*

- (i) *Given a feasible solution  $(\theta, p)$  to MIQ with some spanning tree  $\mathcal{T}$ , then for any spanning tree  $\tilde{\mathcal{T}}$ , there exists a feasible solution  $(\tilde{\theta}, \tilde{p})$  such that  $E_M(\theta, p) = E_M(\tilde{\theta}, \tilde{p})$  and  $\tilde{\theta} = \theta \bmod \frac{\pi}{2}$ .*
- (ii) *Given a feasible solution  $(x, \alpha, \beta)$  to TCO with some choice of basis  $H$ , then for any basis  $\tilde{H}$ , there exists a feasible solution  $(\tilde{x}, \tilde{\alpha}, \tilde{\beta})$ , such that  $E_T(x) = E_T(\tilde{x})$  and  $\tilde{\theta}_T = \theta_T \bmod \frac{\pi}{2}$ .*

This is a straightforward result of Theorem A.1: given a solution  $(\theta, p)$  to MIQ with some spanning tree  $\mathcal{T}$ , we use part (i) of the theorem to construct a solution  $(x, \alpha, \beta)$  to TCO, and then use part (ii) with a *different* spanning tree  $\tilde{\mathcal{T}}$  to construct another MIQ

solution  $(\tilde{\theta}, \tilde{p})$ . The theorem guarantees that  $E_M(\theta, p) = E_M(\tilde{\theta}, \tilde{p})$  and also that  $\tilde{\theta} = \theta \bmod \frac{\pi}{2}$ . A similar argument shows that TCO is invariant to the choice of  $H$ . Note that  $p$  and  $\beta$  might change, though this is inconsequential to the resulting cross fields, which are given by  $\theta$  and  $\theta_T$  respectively.

As the optimization problems are equivalent, we can devise an algorithm for optimizing Equation (3.1) instead of Equation (2.2). There are a few advantages to changing the parameterization of the problem to the variables  $(x, \alpha, \beta)$ . First, we can use the discrete Hodge decomposition [TLHD03] to eliminate the real variables  $x$  and remain with an integer-only problem. Second, the integer variables  $\alpha$  have a geometric meaning, as the cone singularities of the computed cross field, and thus we can devise an efficient iterative method for optimizing them. Finally, the separation of  $\alpha$  and  $\beta$  allows us to relax  $\beta$  while optimizing  $\alpha$ , simplifying the algorithm for high genus meshes.

### 3.2 IOQ

The problem in Equation (3.1) has some interesting properties, as was noted in [CDGDS13, Sec. 8.4.1]. First, recall a fundamental property of the adjacency matrices  $d_0, d_1$ , namely that  $d_1 d_0 = 0$ . Hence, any vector  $x \in \mathbb{R}^l$  can be uniquely decomposed as  $x = d_0 a + B b + d_1^T c$ , where  $B \in \mathbb{R}^{l \times 2g}$  is a matrix whose columns form a basis for the linear space  $\ker(d_1) \setminus \text{im}(d_0)$ , and  $a \in \mathbb{R}^n, b \in \mathbb{R}^{2g}, c \in \mathbb{R}^m$ .  $B$  is computed from  $H$  by  $B = H - d_0(d_0^T d_0)^{\dagger} d_0^T H$  and is orthogonal to  $d_0$  and  $d_1$  (see [CDGDS13, Sec. 8.2.2]). Here  $\dagger$  indicates the Moore-Penrose pseudo-inverse. This decomposition is also known as the Hodge decomposition of discrete differential forms [TLHD03] (we discuss the metric in Section 6.1). Thus, the constraint in Equation (3.1) can be written as:

$$\begin{bmatrix} d_0^T \\ H^T \end{bmatrix} \begin{bmatrix} d_0 & B & d_1^T \end{bmatrix} \begin{bmatrix} a \\ b \\ c \end{bmatrix} = \frac{\pi}{2} s - s_g(\Gamma), \quad (3.2)$$

yielding the constraint matrix

$$\begin{bmatrix} d_0^T d_0 & d_0^T B & d_0^T d_1^T \\ H^T d_0 & H^T B & H^T d_1^T \end{bmatrix} = \begin{bmatrix} d_0^T d_0 & 0 & 0 \\ H^T d_0 & H^T B & 0 \end{bmatrix}. \quad (3.3)$$

Here we used the fact that the matrices  $d_0, B$  are orthogonal, and the fact that the edge values of the non-contractible dual cycles in  $H$  sum to 0 on all triangles; thus  $H^T d_1^T = 0$ . Consequently,  $c$  is not constrained by Equation (3.3). Due to the orthogonality of the decomposition, we have  $E_T(x) = \|d_0 a\|_2^2 + \|B b\|_2^2 + \|d_1^T c\|_2^2$ , and thus the optimal solution will always have  $c = 0$ . Finally, the constraint on  $a$  does not depend on  $\beta$ , and is given by:

$$a(\alpha) = L^{\dagger}(\frac{\pi}{2}\alpha - \alpha_g), \quad (3.4)$$

where  $L = d_0^T d_0$  is the graph Laplacian. Note that  $a(\alpha)$  is defined only up to an additive constant, since  $L$  has co-rank 1. Similarly, the constraint on  $b$  is:

$$b(\alpha, \beta) = (H^T B)^{-1} \left( \frac{\pi}{2} \beta - \beta_g(\Gamma) - H^T d_0 a(\alpha) \right), \quad (3.5)$$

where  $H^T B$  is non-singular since both  $H$  and  $B$  are full rank.

Combining these properties allows us to eliminate the real-valued variables  $a, b$  and remain only with the integer-valued variables  $\alpha, \beta$ . Hence, the part of the objective function that depends on the cone singularities  $\alpha$  is:

$$E_I(\alpha) = \|d_0 a(\alpha)\|_2^2 = \left( \frac{\pi}{2} \alpha - \alpha_g \right)^T L^\dagger \left( \frac{\pi}{2} \alpha - \alpha_g \right), \quad (3.6)$$

where we used the fact that  $L^\dagger$  is symmetric, and  $L^\dagger LL^\dagger = L^\dagger$ . Finally, the optimization problem is:

$$\begin{aligned} & \underset{\alpha \in \mathbb{Z}^n, \beta \in \mathbb{Z}^{2g}}{\text{minimize}} \quad E_I(\alpha, \beta) = E_I(\alpha) + \|Bb(\alpha, \beta)\|_2^2 \\ & \text{subject to} \quad \sum_{i=1}^n \alpha_i = 4\chi. \end{aligned} \quad (3.7)$$

The optimization problems TCO and IOQ are equivalent. Formally, we have:

**Theorem 3.3.**  *$(x, \alpha, \beta)$  is an optimal solution to Equation (3.1) if and only if  $x = d_0 a(\alpha) + Bb(\alpha, \beta)$  and  $(\alpha, \beta)$  is an optimal solution to Equation (3.7).*

The proof is a straightforward result of Equations (3.2)-(3.5) and is provided in the Appendix for completeness. Similar results, albeit not in the context of optimizing the holonomy signature, appear in [CDGDS13, Sec. 8.4.1] and [CZ17a].

**Corollary 3.4.** *For a closed, oriented triangle mesh, with a single directional constraint, the optimal cross field for MIQ, i.e., the optimal  $\theta \bmod \frac{\pi}{2}$  in Equation (2.2), is fully determined by the holonomy signature  $s = [\alpha, \beta]$ .*

This is a straightforward result of Theorem A.1 and Theorem A.2. A solution  $(\theta, p)$  is optimal for MIQ if and only if there exists a corresponding optimal solution  $(x, \alpha, \beta)$  for TCO, where  $(\alpha, \beta)$  are also optimal for IOQ. Thus optimality can be determined from the holonomy signature  $s = [\alpha, \beta]$ .

### 3.3 IOQr: Relaxation

We will consider a relaxation of Equation (3.7), with the  $\beta$  variables relaxed to be real-valued. Note that in this case we can always make  $b(\alpha, \beta)$  equal 0 by taking  $\beta^*(\alpha) = \frac{2}{\pi} (\beta_g(H) + H^T d_0 a(\alpha))$ . Thus, we can eliminate  $\beta$  and solve

$$\begin{aligned} & \underset{\alpha \in \mathbb{Z}^n}{\text{minimize}} \quad E_I(\alpha) \\ & \text{subject to} \quad \sum_{i=1}^n \alpha_i = 4\chi. \end{aligned} \quad (3.8)$$

Then, given the solution  $\alpha^*$  to the above, we further solve:

$$\underset{\beta \in \mathbb{Z}^n}{\text{minimize}} \quad \|Bb(\alpha^*, \beta)\|_2^2. \quad (3.9)$$

In the following two sections we first propose an iterative algorithm for minimizing the energy in Equations (3.8), (3.9) and then show how to devise an approximation that allows us to trade-off the quality of the cross field and the computational time.



## Chapter 4

# Optimization

### 4.1 Solving for $\alpha$

The optimization problem in Equation (3.8) is an instance of the *closest vector problem* (CVP) [Mic01], known to be NP-hard in the general setting. While there exist instances of the problem that are polynomially solvable [SG17], to the best of our knowledge such an algorithm is not currently known for matrices of the form of  $L^\dagger$ . Furthermore, our problem has an additional complication due to the sum constraint on  $\alpha$ . We therefore opt for an *iterative* approach that has some favorable properties: (i) the constraint holds by construction, (ii) it is easily parallelizable, and (iii) it is closely related to the *resistance distance* and thus admits a graph-theoretic approximation.

Assume  $\alpha^{(t)} \in \mathbb{Z}^n$  is a feasible solution for Equation (3.8), and consider the update  $\alpha^{(t+1)} = \alpha^{(t)} + h_{ij}$ , where  $h_{ij} = h_i - h_j$ , and  $h_i \in \mathbb{Z}^n$  is a vector that is all zeros except for a single 1 at the  $i$ -th entry. Note that  $\alpha^{(t+1)}$  sums to  $4\chi$ . Thus, to minimize (3.8), we start with a random feasible  $\alpha^{(0)} \in \mathbb{Z}^n$ , and iteratively update it by adding the best  $h_{ij}$  over all possible choices of  $i, j$ ,  $i \neq j$  as follows:

$$(i^*, j^*) = \arg \min_{1 \leq i, j \leq n, i \neq j} E(\alpha^{(t)} + h_{ij}),$$

$$\alpha^{(t+1)} = \alpha^{(t)} + h_{i^*j^*}.$$

We continue this process as long as there exists a choice of  $(i, j)$  that reduces the energy.

While global optimality cannot be guaranteed, we have some partial guarantees since there is no  $h_{ij}$  that reduces the energy. Specifically, it is easy to see that there is no relocation of a single cone singularity of magnitude  $\pm \frac{\pi}{2}$ , and no cancellation of two such singularities that reduces the energy.

### 4.2 Solving for $\beta$

The optimization problem in Equation (3.9) is also a CVP, of dimension  $2g$ , with the matrix  $\frac{\pi}{2}B(H^T B)^{-1}$  and the target vector  $B(H^T B)^{-1}(\beta_g + H^T d_0 a)$ . For low

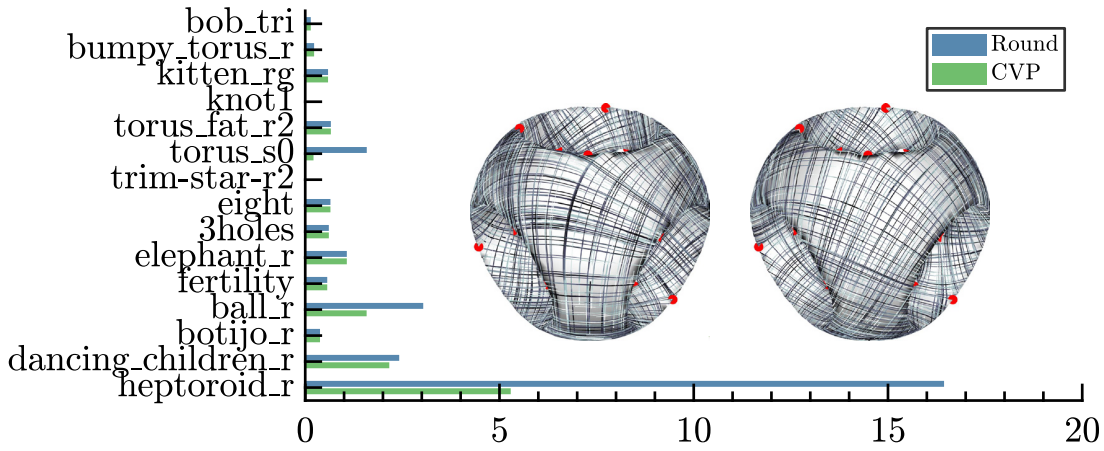


Figure 4.1: Comparison between direct rounding and an exact CVP solver [AEVZ02] for some low resolution meshes sorted by genus. Note that in most cases direct rounding yielded an optimal solution. Notable exceptions are the ball and heptoroid meshes, of genus 5 and 22 respectively, where CVP did improve the solution considerably. We also show the resulting cross fields for the ball mesh with  $\beta$  computed by rounding (left) and CVP (right).

dimensional lattices, and low resolution meshes, i.e. when  $g, n$  are small, finding the optimal solution is still computationally feasible [AEVZ02]. However, we found that direct rounding yields excellent results, and in many cases the exact CVP solution did not considerably improve the energy. This is demonstrated in Figure 4.1, which shows the energy  $\|Bb(\alpha, \beta)\|_2^2$  computed using direct rounding and using the exact CVP solution. Thus, in our experiments we use  $\beta = \text{round}(\beta^*(\alpha^*))$ . A large improvement in the energy did occur for some of the higher genus meshes, implying an interesting future research direction.

### 4.3 Initialization

To initialize  $\alpha^{(0)}$ , we pick a set of random indices  $S \subseteq \{1, \dots, n\}$  and set  $\alpha^{(0)}$  at these locations to  $\pm 1$  such that  $\sum_i \alpha_i^{(0)} = 4\chi$  holds.

To check the stability of our algorithm to this initialization, we ran it on the Bunny mesh with a varying number of initial singularities,  $N = 30$  times for each  $|S|$  value. For each run, we measured the resulting final energy, and the resulting number of cone singularities. As is evident in Figure 4.2, both the energy (left) and the final number of singularities (right) are stable under the choice of initial random input, even when the number of initial singularities is far larger than their final number. For reference, we also show the energy value and the number of singularities of MIQ for this mesh. Note that for all runs our results yield a lower number of singularities and a lower energy.

As the figure shows, there is a larger variability in the final number of singularities than in the energy. We believe this is because there are multiple solutions that lead

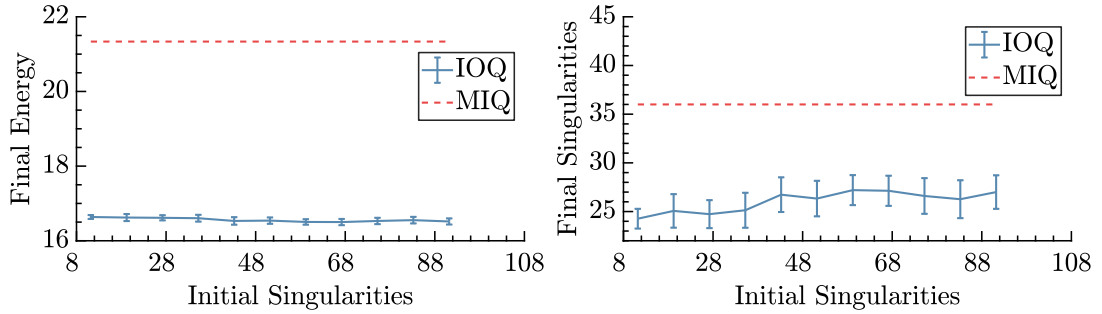


Figure 4.2: Final energy value (left) and final number of cone singularities (right) as we increase the number of initial singularities. We also show the energy value and number of singularities of MIQ [BZK09]. Note that our method is stable to the initialization, and in all cases yields a better energy than MIQ with fewer singularities.

to similar energy values. To demonstrate this, we additionally show in Figure 4.3 the average of  $\alpha$  across all  $N$  experiments for the initial (a) and final (b) iterations. Note that while the singularities concentrate at specific locations, there might be multiple equivalent configurations, e.g. on the tail, leading to a greater variation in the singularities than in the energy. We additionally show one of our results (c), and the MIQ result (d).

#### 4.4 Convergence.

Our algorithm converges in a relatively small number of iterations. Figure 5.2 (left) shows the energy values during the iterations, for different numbers of initial singularities, additional to the minimal number required to fulfill the constraints on  $\alpha$ . Note that starting from more singularities leads to slower conversion; thus, in our experiments we always use for initialization the minimal number possible of  $\pm \frac{\pi}{2}$  singularities.

#### 4.5 Parallelization

Our iterative update for  $\alpha$  is computationally demanding, yet easily parallelizable. To devise a practical algorithm, we note the change in energy due to the addition of  $h_{ij}$ :

$$\frac{\pi^2}{4} E_I(\alpha + h_{ij}) = \frac{\pi^2}{4} (E_I(\alpha) + h_{ij}^T u(\alpha) + R_{ij}),$$

where

$$R_{ij} = h_{ij}^T L^\dagger h_{ij}, \quad u(\alpha) = 2L^\dagger (\alpha - \frac{2}{\pi} \alpha_g).$$

Note that the matrix  $R$ , whose  $(i, j)$ -th entries are given by  $R_{ij}$ , is *independent* of  $\alpha$  and can be precomputed. Furthermore, we have:

$$u(\alpha + h_{ij}) = 2L^\dagger(\alpha - \frac{2}{\pi}\alpha_g + h_{ij}) = u(\alpha) + 2L^\dagger h_{ij}.$$

Thus we can compute  $u^{(0)} = u(\alpha^{(0)})$  and update it at every iteration. Hence, at each iteration we do the following:

$$\begin{aligned} (i^*, j^*) &= \underset{1 \leq i, j \leq n, i \neq j}{\arg \min} u_i^{(t)} - u_j^{(t)} + R_{ij}, \\ \alpha^{(t+1)} &= \alpha^{(t)} + h_{i^*} - h_{j^*}, \\ u^{(t+1)} &= u^{(t)} + 2L_{i^*}^\dagger - 2L_{j^*}^\dagger, \end{aligned}$$

where  $L_i^\dagger$  is the  $i$ -th column of  $L^\dagger$ . The resulting algorithm, denoted IOQr, is given in Algorithm 4.1.

The algorithm is highly parallel, since the computation for every  $(i, j)$  is independent, and thus it is naturally amenable to a GPU implementation. It does, however, require the precomputation of  $L^\dagger$ , which may be prohibitive for large meshes. In our experiments, this algorithm was adequate for meshes with up to  $40K$  faces (see Figure 3 in the supplemental material) on an NVIDIA GeForce GTX 1080 Ti GPU. For larger meshes, we propose an approximation scheme described in the next section.

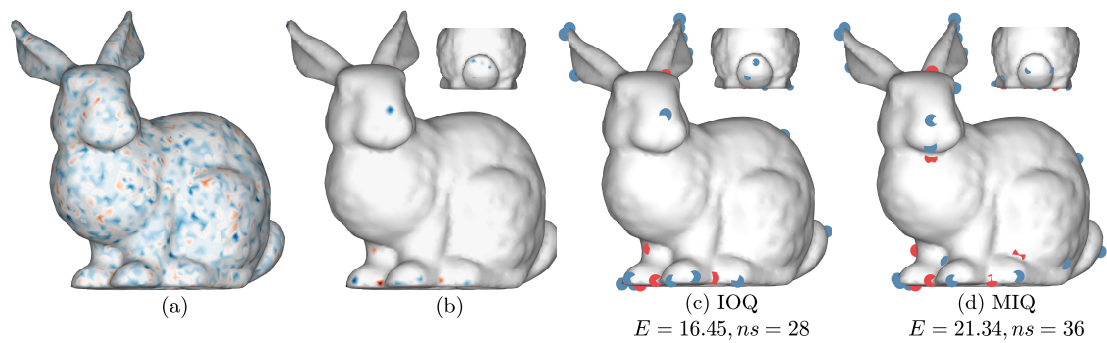


Figure 4.3: The average of  $\alpha$  across  $N$  random initializations for the initial (a) and final (b) iterations. Note that the singularities concentrate at specific locations, yet there might be multiple equivalent configurations, e.g. on the tail. We also show one of our results (c) and the MIQ result (d).

---

**Algorithm 4.1 IOQr, IOQ $\epsilon$**

---

**Input:**  $\mathcal{V}, \mathcal{F}, \mathcal{E}, d_0, H, L^\dagger, R, \tilde{R}_\epsilon$

**Output:**  $\alpha, \beta$

- 1:  $n, m, l \leftarrow$  number of vertices, faces, and edges respectively
  - 2:  $\alpha^{(0)} \leftarrow$  random placement of  $\pm 1$  such that  $\sum_i \alpha_i^{(0)} = 4\chi, \alpha^{(0)} \in \mathbb{Z}^n$
  - 3:  $m^{(0)} \leftarrow -\infty; t \leftarrow 0$
  - 4:  $u^{(0)} \leftarrow 2L^\dagger(\alpha^{(0)} - \frac{2}{\pi}\alpha_g); u^{(0)} = \text{solve}(L, 2\alpha^{(0)} - \frac{4}{\pi}\alpha_g)$
  - 5: **while**  $m^{(t)} < 0$  **do**
  - 6:    $i, j \leftarrow \arg \min_{1 \leq i, j \leq n, i \neq j} u_i^{(t)} - u_j^{(t)} + R_{ij}; \dots + (\tilde{R}_\epsilon)_{ij}$
  - 7:    $\alpha^{(t+1)} \leftarrow \alpha^{(t)} + h_i - h_j$
  - 8:    $u^{(t+1)} \leftarrow u^{(t)} + 2L_i^\dagger - 2L_j^\dagger; u^{(t+1)} = \text{solve}(L, 2\alpha^{(t+1)} - \frac{4}{\pi}\alpha_g)$
  - 9:    $m^{(t+1)} \leftarrow u_i^{(t)} - u_j^{(t)} + R_{ij}; \dots + (\tilde{R}_\epsilon)_{ij}$
  - 10:    $t \leftarrow t + 1$
  - 11: **end while**
  - 12:  $a = \text{solve}(L, \frac{\pi}{2}\alpha^{(t)} - \alpha_g)$
  - 13:  $\beta = \text{round}(\frac{2}{\pi}(\beta_g(H) + H^T d_0 a))$
-



# Chapter 5

## Approximation

### 5.1 Background: The Resistance Distance

The matrix  $R$  that appears in Algorithm 4.1 has a geometric meaning, and is known as the *graph resistance distance* matrix. It encodes graph-theoretical distances originally used in the theory of electrical networks [Kir58]. On an edge, it is equal to the potential difference when we inject a unit current at one end of the edge and extract it at the other end. It can also be thought of as the commute time between two vertices [CRR<sup>+</sup>96], or the probability that an edge appears in a random spanning tree of the graph [DS84, Bol13]. The resistance distance, also known as the *commute time distance*, has been used in geometry processing for various applications; see e.g. [PS13]. It can be computed explicitly by:

$$R_{ij} = h_{ij}^T L^\dagger h_{ij} = L_{ii}^\dagger + L_{jj}^\dagger - 2L_{ij}^\dagger,$$

yet this requires the matrix  $L^\dagger$ , which is computationally prohibitive to compute for large meshes. To overcome this, we use an efficient random approximation of  $R$ .

---

**Algorithm 5.1** Approximate resistance distance

---

**Input:**  $\mathcal{V}, \mathcal{E}, \epsilon$

**Output:**  $\tilde{R}_\epsilon$

- 1:  $k \leftarrow \text{round}(24 \log n / \epsilon^2)$
  - 2:  $Q \leftarrow \text{random } k \times l \text{ matrix with entries } \pm 1/\sqrt{k}$
  - 3:  $Y \leftarrow Qd_0$
  - 4:  $Z^T = \text{solve}(L, Y^T)$
  - 5:  $(\tilde{R}_\epsilon)_{ij} = \|Z_i - Z_j\|_2^2$
- 

### 5.2 Random Approximation

Spielman and Srivastava [2011] proposed a method, based on random projections, to approximate the resistance distance of a given graph. Calculating  $R$  is equivalent to

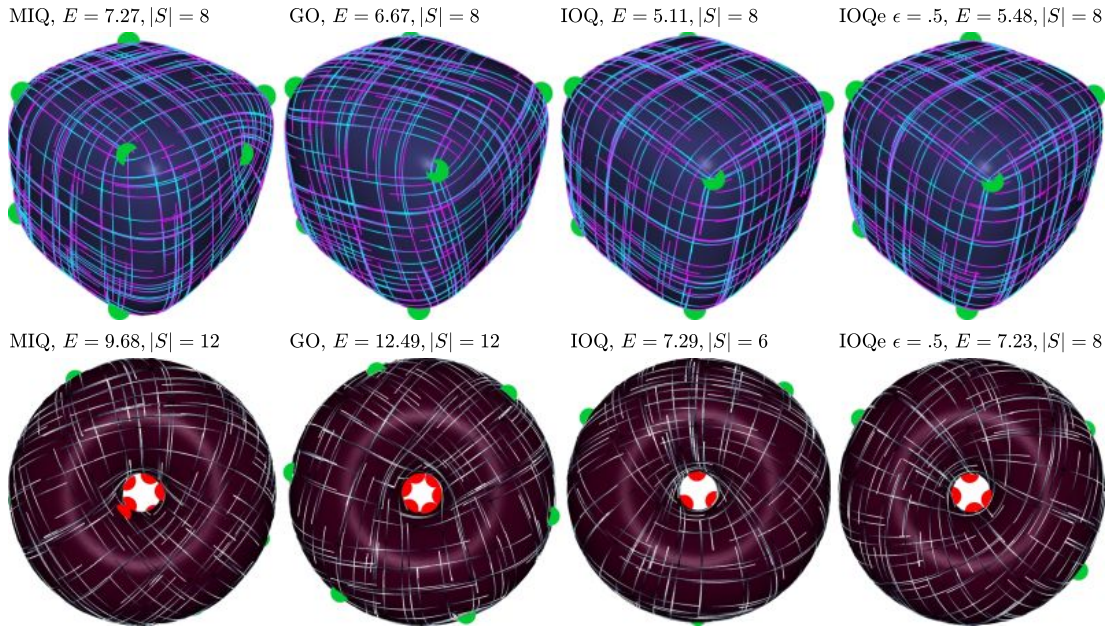


Figure 5.1: The results of our exact and approximated algorithms (IOQ and IOQe), compared with MIQ [BZK09] and GO [KCPS13], on two symmetric models. See the text for details.

computing the pair-wise Euclidean distances between points in  $\{d_0 L^\dagger h_i\}_{v_i \in \mathcal{V}}$ , which are the columns of  $d_0 L^\dagger$ . This is true since

$$\begin{aligned} R_{ij} &= h_{ij}^T L^\dagger h_{ij} = h_{ij}^T L^\dagger L L^\dagger h_{ij} \\ &= (h_{ij}^T L^\dagger d_0^T) (d_0 L^\dagger h_{ij}) = \|d_0 L^\dagger h_{ij}\|_2^2. \end{aligned}$$

To efficiently and accurately approximate these, Spielman and Srivastava [2011] projected the columns of  $d_0 L^\dagger$  onto a subspace spanned by  $O(\log n)$  random vectors and calculate the distances in the *projected space*. Let  $Q_{k \times l}$  be a random *Bernoulli* matrix with entries of  $\pm 1/\sqrt{k}$ , where  $k \geq 24 \log n/\epsilon^2$ , for some  $\epsilon > 0$ . They computed  $Y = Qd_0$  and solve  $ZL = Y$  for  $Z$ . The  $n$  columns of  $Z$  are the projected points of dimension  $k$ , and we can use the Euclidean distances between them to approximate the resistance distance by:

$$(\tilde{R}_\epsilon)_{ij} = \|Z_i - Z_j\|_2^2,$$

where  $Z_i$  is the  $i$ -th column of  $Z$ . The algorithm for computing  $\tilde{R}_\epsilon$  is provided in Algorithm 5.1.

**Implementation.** Spielman and Srivastava [2011] in fact further speed up the theoretical running time by approximating  $Z$  using [ST04, ST14], but we found this step to be unnecessary since the computation time was dominated by computing  $\tilde{R}_{ij}$  for all  $i, j \in \mathcal{V}$ , whereas in Spielman and Srivastava [2011] they compute it only for  $e_{ij} \in \mathcal{E}$ .

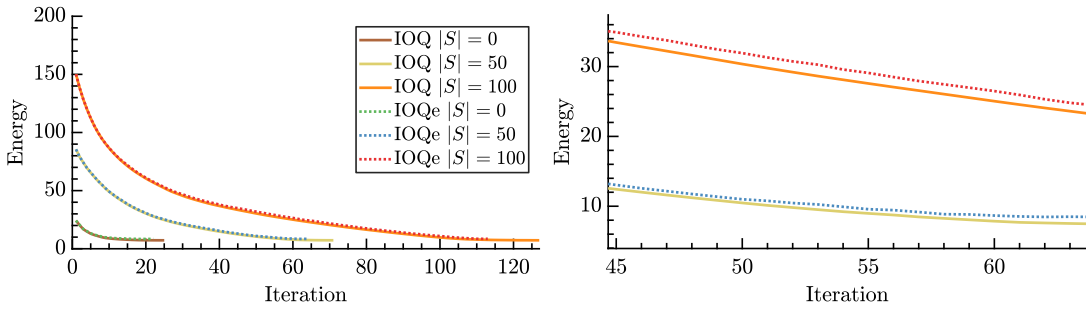


Figure 5.2: Left: Energy values during the iterations for different numbers of initial singularities, for both the exact (IOQ) and approximated (IOQe) methods. Right: Close-up of the same graph. Note that the energy plot of the approximated method is nearly indistinguishable from the exact method.

To compute  $Z$  we first factorize  $L$ , and then use back-substitution, using [Dav13]. The pair-wise distances between all the columns in  $Z$  are then computed efficiently on the GPU using the built-in Matlab function “`pdist`”. The algorithmic modifications required in order to work with the approximate resistances instead of  $R$  and  $L^\dagger$  are minor. The only difference is that instead of using  $L^\dagger$  for updating  $u$ , we need to solve a sparse linear system at every iteration, yet we can do that efficiently using the factorization of  $L$ . The changes are highlighted in Algorithm 4.1, where green lines replace blue lines when using approximate resistances. Note that when using approximate resistances, the energy is no longer guaranteed to monotonically decrease; thus, we stop when we identify a cycle in the solutions.

Figure 5.2 shows the energy values during the iterations for the approximated and exact algorithms with the same initialization. Note that the graphs are almost indistinguishable. Indeed, in practice the approximated algorithm yields energy values that are very close to the result of the exact algorithm. Figure 5.1 shows the output of the approximated algorithm with  $\epsilon = 0.5$  compared with MIQ [BZK09], GO [KCPS13] and our exact algorithm IOQ, on two symmetric models. Note that compared to MIQ and GO on the torus, IOQ finds a lower energy solution with fewer singularities. Furthermore, for both the cube and the torus, the singularities’ locations are close to symmetric. IOQe yields very similar results to IOQ, at the expense of a slightly higher energy. Note that the GO result on the cube is very similar to ours, up to a global rotation of all the crosses, which does not affect the energy.

**Approximation quality.** The Johnson-Lindenstrauss Lemma guarantees that with high probability the Euclidean distances will not be distorted by more than a multiplicative factor of  $1 \pm \epsilon$  [JL84, Ach01, DG03]. In practice, we found that for graphs that come from triangle meshes, the distortion is empirically less than the theoretical guarantee. Figure 5.3 (left) shows the distortion ratio of  $R_{ij}/(\tilde{R}_\epsilon)_{ij}$  for different values of  $\epsilon$ . For example, for  $n=55,000$  and  $\epsilon \approx 0.5$ , the reduced dimension is  $k=1000$ . In this

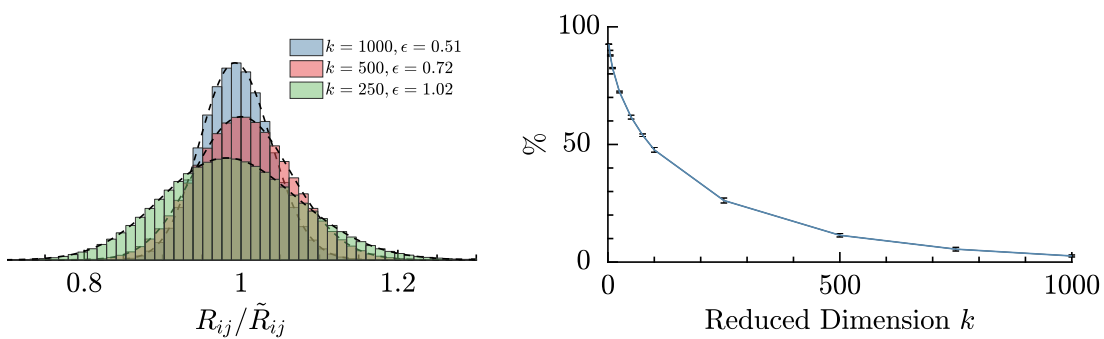


Figure 5.3: Left: Histogram of the pair-wise distortions  $R_{ij}/(\tilde{R}_e)_{ij}$  for three values of  $\epsilon$ . Right: Percentage of pairs with distortion greater than 10% as we increase the projected dimension  $k$ . See the text for details.

case, the expected distortion is 50%, yet the actual observed maximal distortion is only around 15%. In Figure 5.3 (right) we show the trend for a growing  $k$ , i.e. a decreasing  $\epsilon$ , of the percentage of pairs with distortion higher than 10%, again for  $n = 55,000$ . Note that the distortion quickly decreases, with less than 5% of such pairs for  $k = 1000$ .

To give some insight into the behavior of the approximation, we visualize in Figure 5.4 the exact resistance distance  $R$ , and its approximation  $\tilde{R}_\epsilon$  for different values of  $\epsilon$ . We show these as color coded functions, where the function is the resistance distance of all mesh vertices from a single marked vertex. Note that, as expected, the functions become noisier as  $\epsilon$  grows, yet qualitatively, they are similar to the exact resistance distance.

**Time/quality tradeoff.** Fig. 5.5 shows the robustness of this approximation when combined with our algorithm, and the resulting trade-off between the quality of the output and the computational time. We first compute  $N = 300$  different  $\tilde{R}_\epsilon$  for various  $\epsilon$  values, by running Algorithm 5.1. Then, for a fixed initial  $\alpha^{(0)}$ , we run Algorithm 4.1 with the different  $\tilde{R}_\epsilon$ . We show in (b-d) the average optimal  $\alpha$  after convergence, where

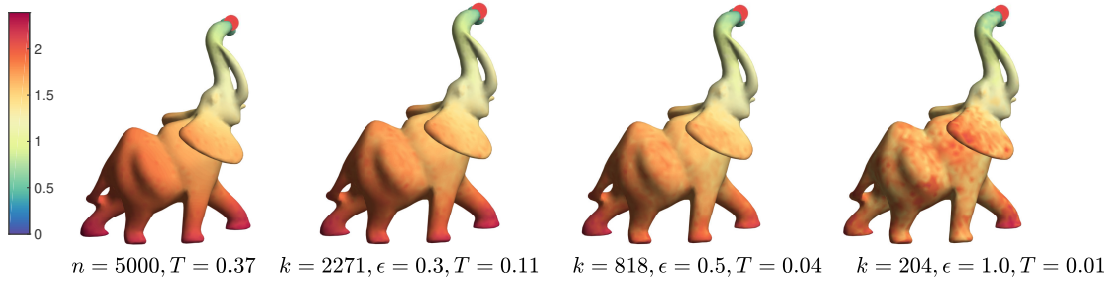


Figure 5.4: The resistance distance and its approximations as we increase  $\epsilon$ , with respect to the red point. Here we show the running time in seconds,  $T$ , and the original and projected dimension,  $n$  and  $k$  respectively.

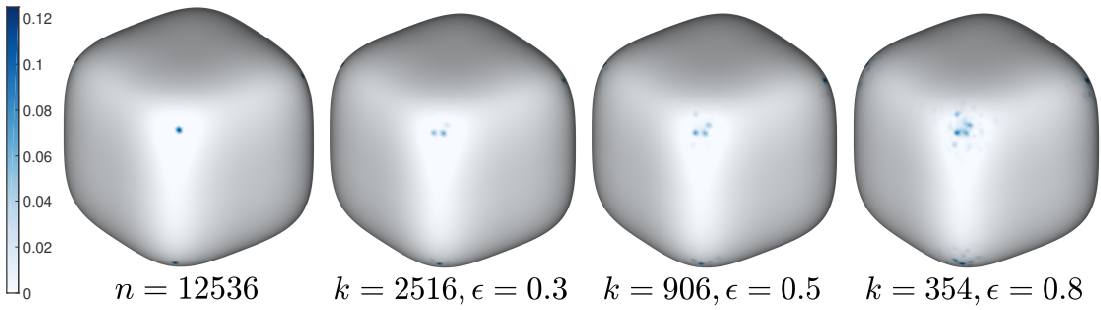


Figure 5.5: Time/quality tradeoff of IOQ $\epsilon$  with different  $\epsilon$  values. We show the average across  $N = 300$  experiments of  $\alpha$  after convergence, using (a) the exact resistance distance with different initial random  $\alpha$ ; and (b-d) the approximate resistance, with different random projections and the same initial  $\alpha$ . Note that for  $\epsilon = 0.5$  we get a dimensionality reduction of more than 90%, yet the algorithm yields excellent cone positions.

we average across the  $N$  experiments for matrices with the same  $\epsilon$ . In addition, we show in (a) the average optimal  $\alpha$ , when using the exact resistance distance, and starting from  $N$  random initializations, for comparison. As the figure shows, while the locations of the singularities degrade for very large  $\epsilon$ , for  $\epsilon = 0.5$  we achieve a dimensionality reduction of more than 90%, and still get an excellent distribution of the locations of the singularities. In all our experiments, unless mentioned otherwise, we used  $\epsilon = 0.5$ .



# Chapter 6

## Implementation

We implemented our algorithm in Matlab, using its built-in support for GPU parallelization with “gpuArray”. For the inner loop that minimizes over all  $(i, j)$  pairs, we used a CUDA kernel. For the exact algorithm, we first attempt to compute  $L^\dagger$  on the GPU, and if that fails due to memory requirements, we attempt a blockwise GPU inversion. If that also fails, we invert  $L^\dagger$  on the CPU. For large meshes, where  $L$  cannot be inverted on the GPU, the exact algorithm is therefore computationally very expensive. For the approximate algorithm, we factorize  $L$  on the CPU, and use the factorization to compute  $Z$ . Then  $\tilde{R}_\epsilon$  is computed from  $Z$  on the GPU. On our machine, with an NVIDIA GeForce GTX 1080 Ti GPU and an Intel Core i7-7820X CPU @ 3.60GHz with 8 cores, the exact algorithm takes a few minutes for a mesh with  $50K$  faces, and the approximate algorithm with  $\epsilon = 0.5$  takes around 20 seconds. The full timing details are provided in Figure 3 of the supplemental material.

### 6.1 Limitations

The main limitation of our algorithm is the heavy computational load. Because we have to fit  $L^\dagger$  or  $R$  on the GPU, the memory requirement is  $O(n^2/2)$ , which on our hardware (12 GB RAM) was feasible for meshes with up to  $100K$  faces. This could potentially be reduced to  $O(n \log(n))$  by holding  $Z$  instead on the GPU and computing  $\tilde{R}_\epsilon$  on the fly.

Another limitation is that we do not handle directional constraints. In many scenarios, especially quadrangular remeshing, it is beneficial if the cross field is aligned with the curvature directions of the surface. We leave the generalization of our approach to directional constraints for future work.

Finally, the geometry of the surface is not incorporated in the system matrix  $L$ , since we use  $L = d_0^T d_0$ , and not a weighted Laplacian. The TC formulation allows for adding weights on the edges, [CDS10, Section 2.5], and a similar approach could be applied to MIQ as well. We did not attempt that, as we wished to compare to a non-modified MIQ. As the approach of Spielman and Srivastava [2011] can be applied to a weighted graph, we believe a suitable adaptation of our algorithm that incorporates the geometry

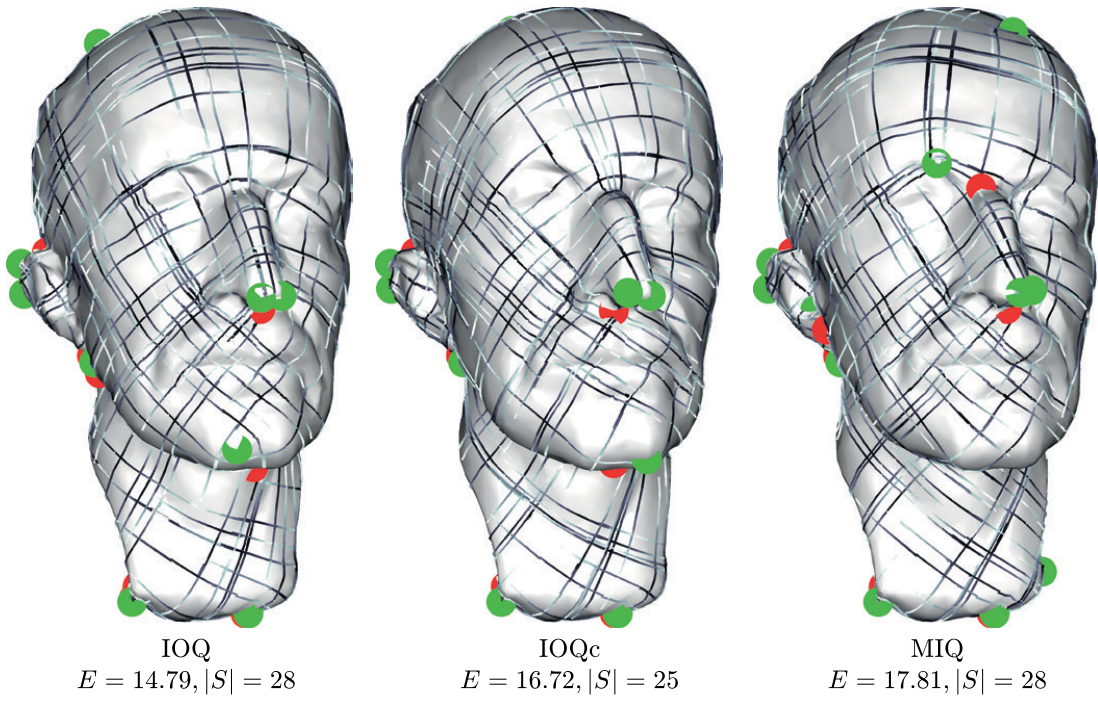


Figure 6.1: An example of our method with the graph Laplacian (left) and the cotangent Laplacian (middle) compared to MIQ (right). Note that in both cases our method finds a better solution in terms of smoothness energy and singularity placement.

in  $L$  can be devised. See Figure 6.1 for a preliminary result in which we replaced  $L$  by the cotangent Laplacian and no approximation was used. Note that the resulting cross-field has fewer singularities and a lower smoothness energy than the MIQ result.

## 6.2 Results

### 6.2.1 Comparisons

**Quantitative, with MIQ [BZK09]** We compared our exact method (IOQ), our approximated method (IOQe with  $\epsilon = 0.5$ ) and MIQ [BZK09]. For IOQ, IOQe and MIQ we used the same single directional constraint on an arbitrary face. GO can be computed without any directional constraints. To evaluate the methods, we assessed the angle-based energy of the output fields  $E = E_M(\theta, p)$  from Equation (2.2), the number of singularities  $|S|$ , i.e. the number of vertices  $v_i \in \mathcal{V}$  such that  $\alpha_i \neq 0$ , and the timing, on the models from the benchmark provided by [MPZ14]. We implemented our method in Matlab and CUDA, while for MIQ we used the Libigl [JP<sup>+</sup>16] implementation.

Figure 6.2 shows the ratio of improvement of our methods vs. the MIQ result, i.e.  $(E_{MIQ}/E_{ours})((|S|_{MIQ} + 1)/(|S|_{ours} + 1))$ . As the figure shows, the product of these ratios is always greater than 1 (the vertical black line); thus, for all models we improve upon MIQ. Also note that the approximate method (IOQe) yields comparable, and

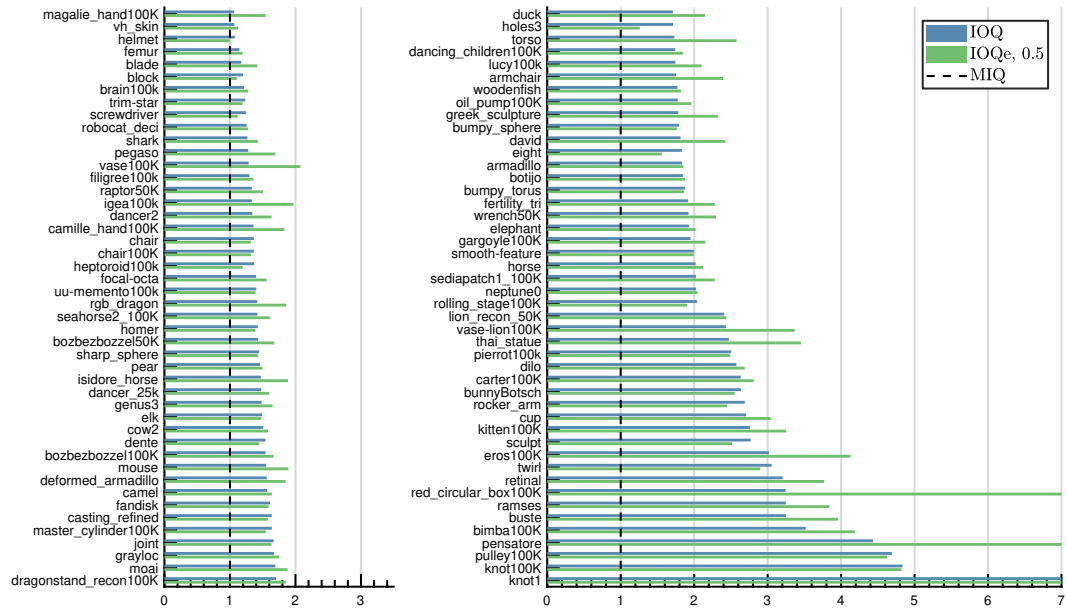


Figure 6.2: The improvement in energy and singularities of our exact (IOQ) and approximate (IOQe) methods relative to MIQ, computed by  $(E_{MIQ}/E_{ours})((|S|_{MIQ} + 1)/(|S|_{ours} + 1))$  on the meshes from [MPZ14], where  $|S|$  is the number of singularities. Note that for all meshes our result is bigger than 1, and thus improves on MIQ. Furthermore, the results of IOQ and IOQe are comparable for most meshes.

sometimes better, results than IOQ. The median improvement ratio over all models is 1.71 for IOQ and 1.86 for IOQe.

**Quantitative, with GO [KCPS13]** The cross field generation method suggested by Knöppel et al. [2013] optimizes a different energy than MIQ, yet is very efficient and has global optimality guarantees (for their energy). We compared our method with GO as well, using a Matlab implementation with a face-based discretization as done in [DVPSH14]. The results are shown in Figure 6.3, using the same quantitative measures as in Figure 6.2. Since we are measuring an energy that GO is not optimizing for, our method outperforms GO in terms of energy. Note, however, that we also outperform GO in terms of the number of singularities. The median improvement rate over all models was 2.99 for IOQ and 3.3 for IOQe. All the quantitative results, i.e.  $E$ ,  $|S|$  for all the methods and all the models are provided in Figures 1 and 2 in the supplemental material.

**Timing.** Our approach is considerably slower than both MIQ and GO. For example, MIQ completed for all the models within a few seconds, whereas GO is even faster, finishing in less than a second for all models. Our approximated method with  $\epsilon = 0.5$  takes around 20 seconds on models of size  $50K$  faces. Our exact method can take around 5 minutes for such models and around 20 minutes for models of  $100K$  faces.

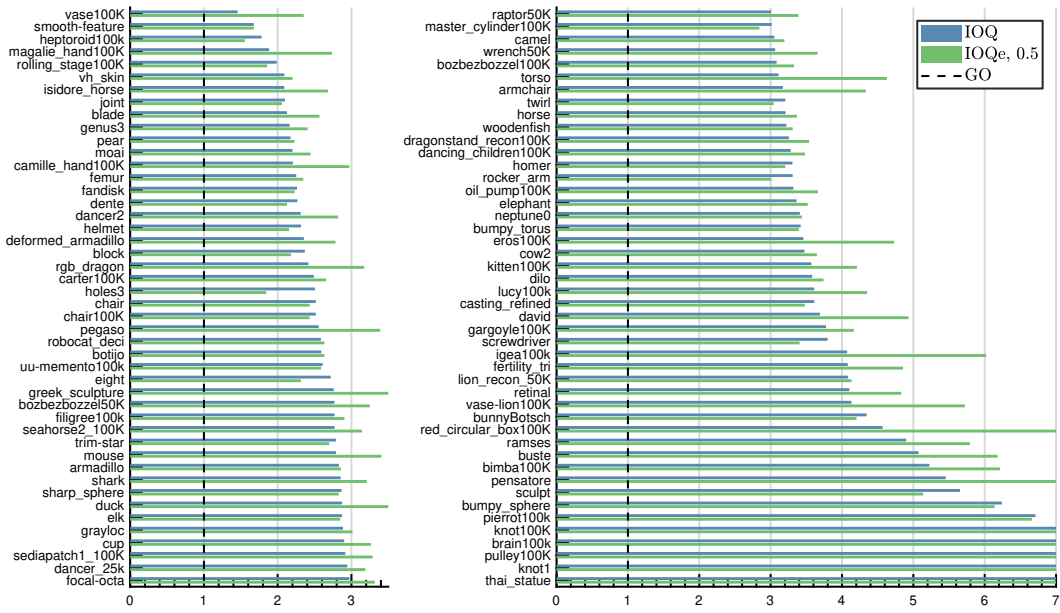


Figure 6.3: The improvement in energy and singularities of our exact (IOQ) and approximate (IOQe) methods relative to GO [KCPS13], using the same protocol as in Figure 6.2. Here, again, for all meshes our result is bigger than 1, and thus improves on GO. Furthermore, the results of IOQ and IOQe are comparable for most meshes.

However, it is efficient for models whose  $L$  matrix can be inverted on the GPU. All the timing results for IOQ and IOQe are provided in Figure 3 in the supplemental material.

**Qualitative.** Figure 6.4 shows a few example models from the benchmark with their corresponding cross fields for the different methods. Note that for the IOQ approach there are considerably fewer singularities, with a smaller energy, and the singularities are well distributed when compared with the MIQ and GO results.

### 6.2.2 Scalability

To compare the scalability of our approach with respect to the energy, number of singularities and timing, we ran our methods and MIQ on a series of meshes with the same geometry and varying resolution of the Bunny mesh. As Figure 6.5 shows, our energy remains the same order of magnitude when increasing the mesh size, and the number of singularities remains largely the same. In terms of timing, both IOQ and IOQe are slower than MIQ, yet IOQe is considerably faster than IOQ.

### 6.2.3 Varying $\epsilon$

Figure 6.6 shows our results on a model with sharp features as we increase  $\epsilon$ , the approximation parameter. Note that with  $\epsilon = 1$ , which reduces the dimension to a mere 3% of the original dimension, IOQe still finds a similar singularity placement, albeit

with a somewhat higher energy. For the best trade-off between the resulting smoothness energy and the reduced dimension, we have found that taking  $\epsilon = 0.5$  is appropriate.

#### 6.2.4 Stability to Noise

To measure the stability of our approach to geometric noise, we added random Gaussian noise in the normal direction to the kitten model, with standard deviation of 10 and 15 percent of the average edge length. The results are shown in Figure 6.7, for IOQe with  $\epsilon = 0.5$  (first three from the left) and MIQ (last three from the right). Note that for the 10 percent noise level the number of singularities remains almost the same for our approach. Even for the higher noise level, our algorithm yields considerably fewer singularities than MIQ, as well as a lower energy.

In another experiment, we randomly flipped the edges of a mesh to get a non-uniform triangulation. While the geometry is not encoded in the system matrix  $L$ , it does contribute to the right hand side of the system through the angle defects  $\alpha_g, \beta_g$ . Therefore, the results are, at least to some extent, robust to changes in the triangulation, as is shown in Figure 6.8.

#### 6.2.5 Application to Quadrangulation

The cross fields we generate can be used for computing quadrangular meshes, by creating a parameterization whose gradients align with the cross directions, and then extracting the quads. We used off-the-shelf approaches for these steps: the parameterization part of MIQ [BZK09, Sec. 5] as implemented in libigl [JP<sup>+</sup>16], and the quad extraction method QEx [EBCK13] that receives as input a parameterization. While in general curvature direction alignment is often required for quad meshing, it seems that in some cases good cone point locations can lead to high quality quadrangular meshes even without alignment. Figure 6.9 shows some examples of quad meshes computed using our cross fields, and using the cross field generated by MIQ. Note that the better placed singularities and lower energy of our approach lead to smoother, more symmetric quad meshes with better shaped quads.

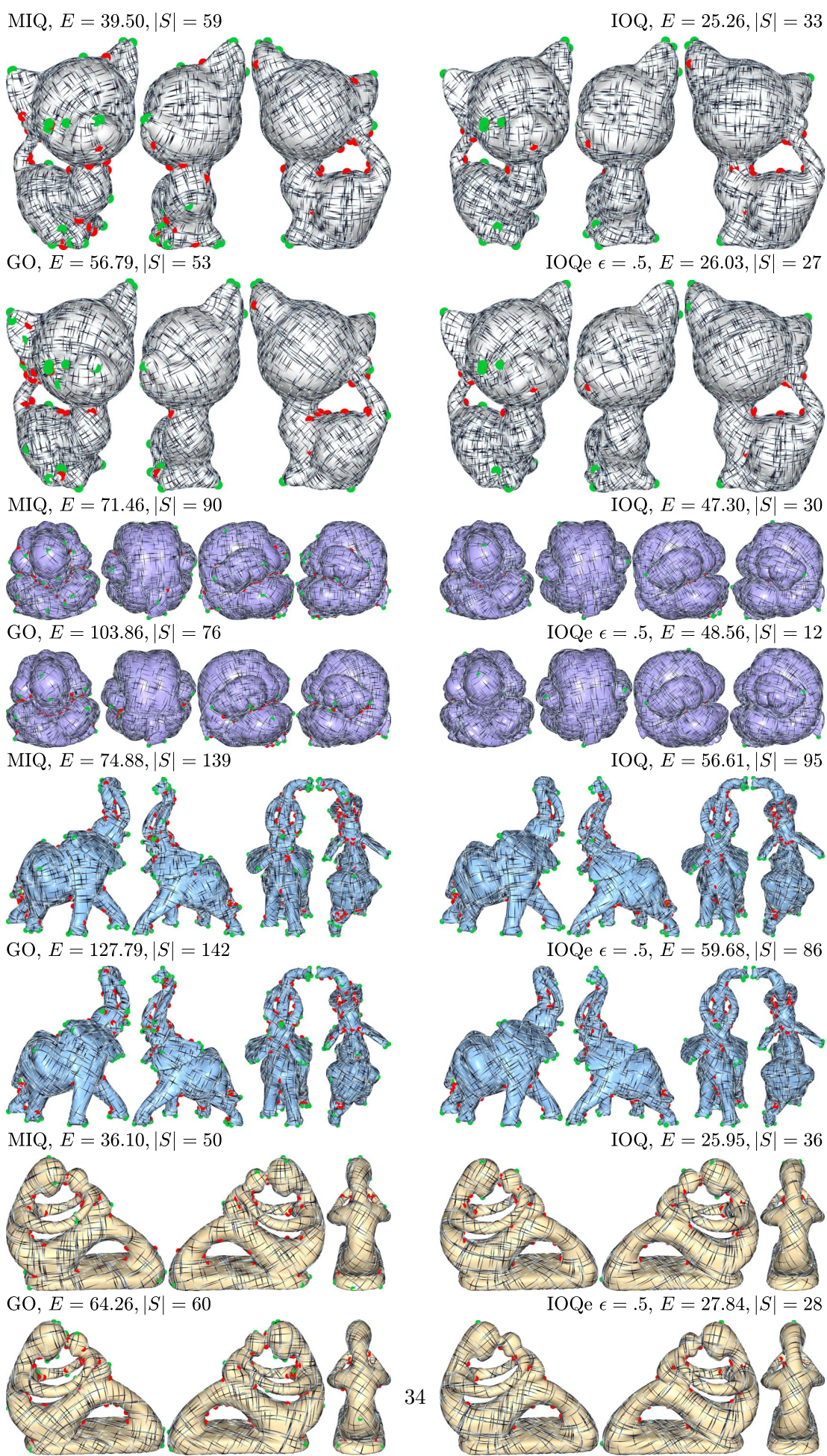


Figure 6.4: Some meshes from the benchmark and their cross fields. Note that our method yields considerably fewer singularities with lower energy values.

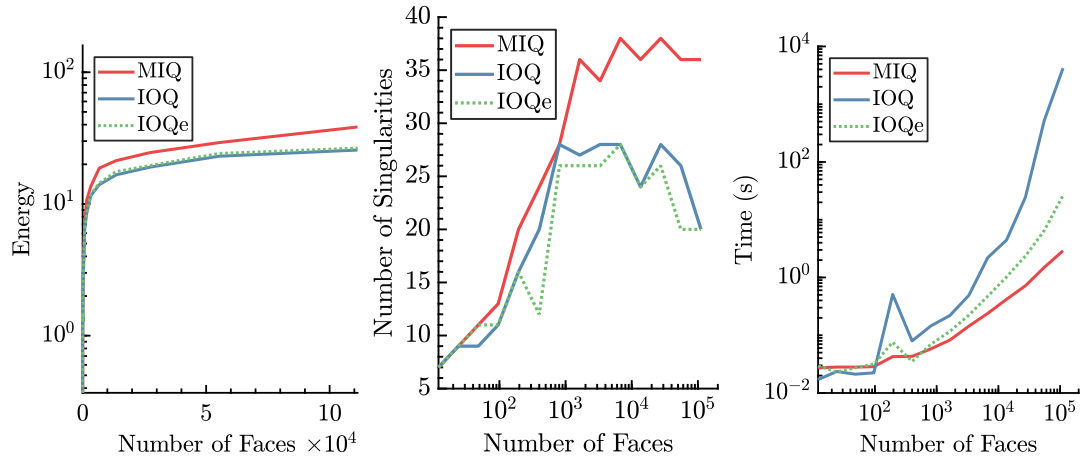


Figure 6.5: Energy, number of singularities and timing scalability, on a series of meshes with varying resolutions. See the text for details.

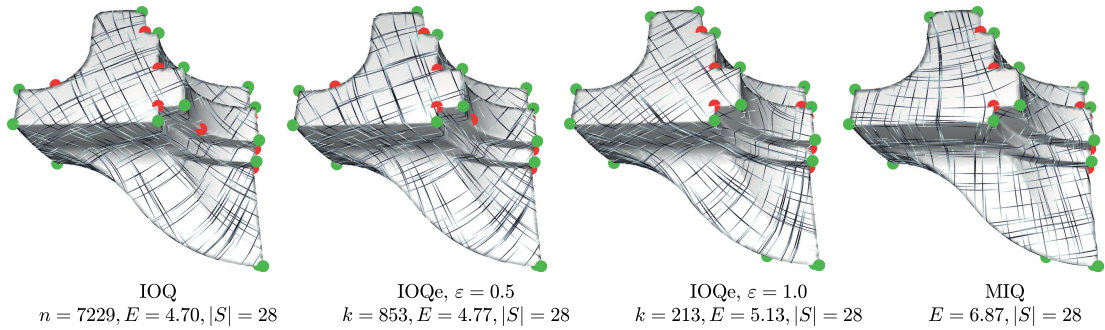


Figure 6.6: Varying the approximation parameter,  $\epsilon$ , has little effect on the final singularity placement. Note in particular that even with a projected dimension of  $k = 213$ , our method still places most of the singularities on the corners as desired, albeit with a somewhat higher energy.

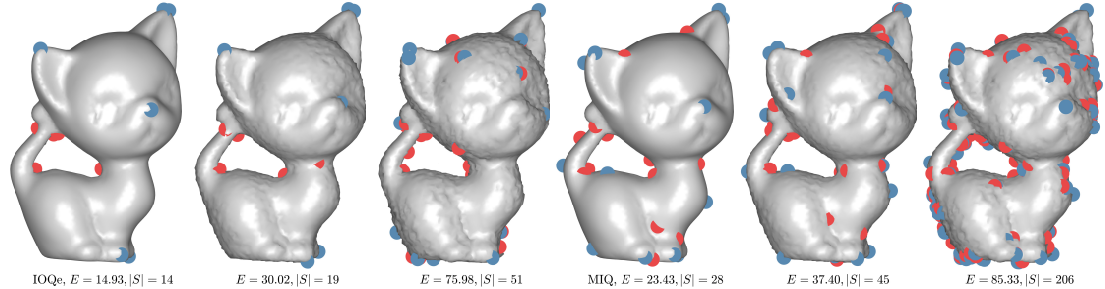


Figure 6.7: Stability of our method (left) compared to MIQ (right) with increasing levels of normal noise added to the vertex positions.

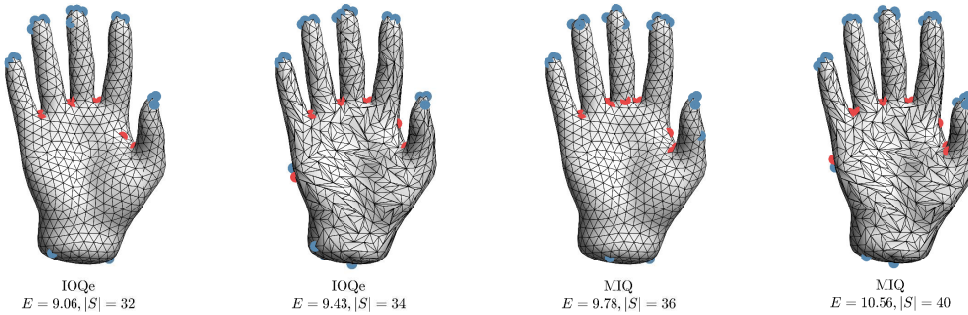


Figure 6.8: The results of our method (left) compared to MIQ (right) on a uniform and non-uniform triangulation. Note that while our method does not incorporate the geometry in the system matrix  $L$ , it is, at least to some extent, robust to changes in the triangulation.

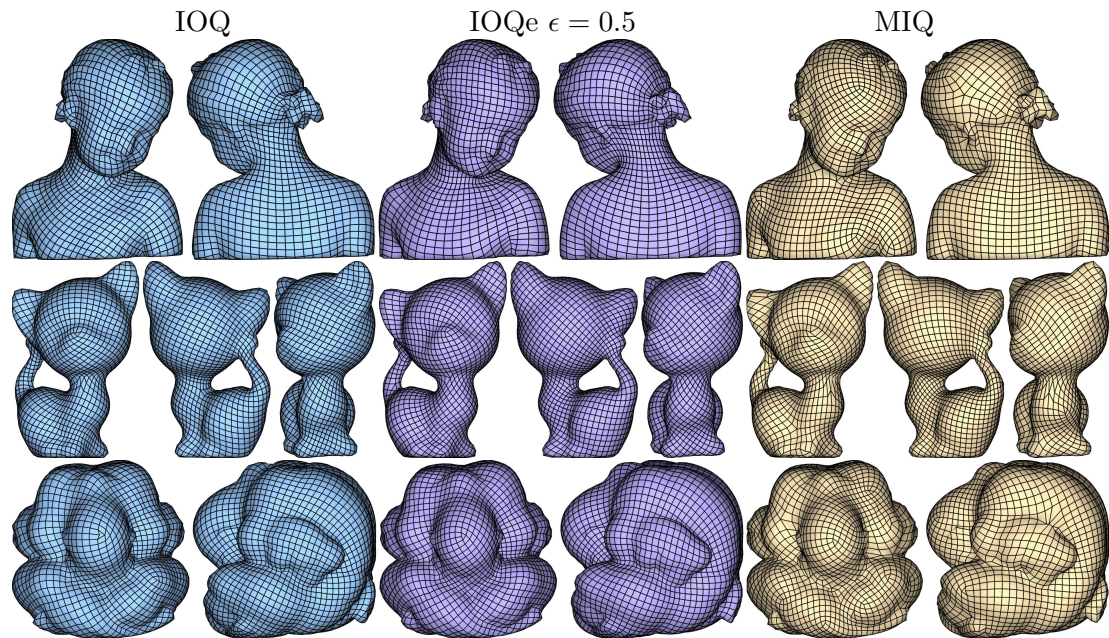


Figure 6.9: Quadrangular meshes generated from our cross fields (left,center), compared to quad meshes generated from MIQ cross fields (right).

## Chapter 7

# Conclusion

We showed an equivalence between two existing methods for generating cross fields, which we then used to formulate a new iterative algorithm that finds better solutions than state-of-the-art results in terms of the angle-based energy and number of singularities. Using a recent approximation of the resistance distance, based on random projections, we allow a trade-off between the computation time and the smoothness of the produced field using a single tunable parameter,  $\epsilon$ .

A natural generalization of our approach is to add support for directional constraints. In addition, we believe that a similar iterative approach could be useful for computing a parameterization with integer cone locations that is aligned with a given cross field. Finally, to the best of our knowledge, this approximation of the resistance distance has not been used in geometry processing, but we posit that it is of independent interest and could be useful in other applications.



## Appendix A

### Appendix - Proofs.

Let  $H \in \mathbb{Z}^{l \times 2g}$  be any integral basis for the non-contractible dual cycles of  $\mathcal{M}$ , e.g. as obtained by computing the tree-cotree decomposition [Epp03, Lemma 3.2] and orienting the edges [CDS10, Sec 2.1], and let  $d_1 \in \mathbb{Z}^{m \times l}$  be the signed face-edge adjacency matrix. Further, let  $\mathcal{T} \subset \mathcal{E}^*$  be a dual spanning tree of  $\mathcal{M}$ .

First, we relate an MIQ solution  $(\theta, p)$  and a TC solution  $(x, \alpha, \beta)$  through the following system of linear equations:

$$\frac{\pi}{2}(\Gamma p + s) = s_g(\Gamma) - \Gamma r, \quad (\text{A.1})$$

$$\frac{\pi}{2}p + d_1^T \theta + x = -r, \quad (\text{A.2})$$

where  $\Gamma^T = [d_0, H]$ ,  $s = [\alpha, \beta]$ , and  $s_g = s_g(\Gamma) = [\alpha_g, \beta_g(H)]$ .

**Lemma A.0.1.** *For any choice of  $H$ , we have that  $I_0(\Gamma) = \frac{2}{\pi}(s_g(\Gamma) - \Gamma r) \in \mathbb{Z}$ , and  $\sum_{i=1}^n I_0(\Gamma)(i) = 4\chi$ .*

**Proof.** By definition,  $s_g(\Gamma)$  are the geometric angle defects around the cycles of  $\Gamma$ , and  $\Gamma r$  is the *holonomy* of the local reference frame field along the cycles of  $\Gamma$  (see, e.g. [CDS10, Sec. 3.2]). Hence, their difference is a multiple integer of  $\frac{\pi}{2}$  and thus  $I_0 \in \mathbb{Z}$ . Furthermore, for  $i = 1..n$  we have that  $I_0(i)$  is the index of the reference frame field at the vertex  $v_i \in \mathcal{V}$ , and thus  $\sum_{i=1}^n I_0(\Gamma)(i) = 4\chi$  [RVLL08, Theorem 2.3].

**Lemma A.0.2.** *Given a dual spanning tree  $\mathcal{T} \subset \mathcal{E}^*$ , let  $\Gamma_f$  be the matrix formed by the columns of  $\Gamma$  corresponding to  $\mathcal{E}^* \setminus \mathcal{T}$ , i.e. dual edges not in  $\mathcal{T}$ . In addition, let  $s \in \mathbb{Z}^{n+2g}$  such that  $\sum_{i=1}^n s_i = 4\chi$ . Then the linear system*

$$\Gamma_f p_f = -s + I_0(\Gamma) \quad (\text{A.3})$$

*has a unique integer solution.*

**Proof.** Every column of  $d_0^T$  sums to 0, thus we can remove its first row and it will still span all the dual cycles. Given a matrix  $M$ , let  $\hat{M}$  denote the matrix with the first row removed. Hence,  $\hat{\Gamma}$  is an integral basis for the dual cycles, with independent rows. Using [LR07, Lemma 27], we have that the matrix  $\hat{\Gamma}_f$  is a non-singular unimodular matrix. Furthermore, the right hand side of Equation (A.3) is integer, since  $s$  is integer and due to Lemma A.0.1. Thus the system  $\hat{\Gamma}_f p_f = -\hat{s} + I_0(\hat{\Gamma})$  has a unique integer solution. Finally, we have that  $\sum_{i=1}^n I_0(\Gamma)(i) = 4\chi$  from Lemma A.0.1, and  $\sum_{i=1}^n s_i = 4\chi$ . Thus  $\sum_{i=1}^n (-s_i + I_0(\Gamma)(i)) = 0$ . Furthermore,  $\sum_{i=1}^n \Gamma_f(i,:) p_f = 0$ , thus,  $p_f$  fulfills the first linear constraint as well, and is thus a unique integer solution of Equation (A.3) as required.

**Lemma A.0.3.** *Let  $(\theta, p)$  be a feasible solution of Equation (2.2) and let  $H$  be an integral basis of non-contractible dual cycles. Then there exists a unique solution  $(x, s)$  of the system of equations (A.1), (A.2) such that  $s = [\alpha, \beta]$  and  $(x, \alpha, \beta)$  is feasible for (3.1).*

**Proof** Let  $s = I_0(\Gamma) - \Gamma p$ , then Equation (A.1) holds for  $(s, p)$ . Note that  $I_0(\Gamma)$  is integer due to Lemma A.0.1, and  $\Gamma p$  is integer since  $\Gamma$  and  $p$  are both integer. Thus,  $s$  is integer. Let  $[\alpha, \beta] = s$ , with  $\alpha \in \mathbb{Z}^n, \beta \in \mathbb{Z}^{2g}$ . Then,  $\alpha = I_0(d_0^T) - d_0^T p$ , namely  $\alpha$  is a vector containing the indices of the cross field  $(\theta, p)$  [BZK09, Sec 4.1], and thus  $\sum_{i=1}^n \alpha_i = 4\chi$  [RVLL08, Theorem 2.3].

Let  $x = -r - \frac{\pi}{2}p - d_1^T \theta$ , then Equation (A.2) holds for  $(x, \theta, p)$ . Now, we have that  $\Gamma x = -\Gamma r - \frac{\pi}{2}\Gamma p - \Gamma d_1^T \theta$ . Note that  $d_1 \Gamma^T = 0$ , since  $d_1 d_0 = 0$ , and the columns of  $H$  are *closed discrete one-forms* (see e.g. [CDGDS13, Sec. 8.2.2]). From Equation (A.1) we have that  $-\Gamma r - \frac{\pi}{2}\Gamma p = \frac{\pi}{2}s - s_g(\Gamma)$ , thus  $\Gamma x - \frac{\pi}{2}s = -s_g(\Gamma)$  and  $(x, s)$  is feasible for the problem (3.1).

**Lemma A.0.4.** *Let  $(x, \alpha, \beta)$  be a feasible solution of Equation (3.1) with cycle basis  $H$ , and let  $\mathcal{T}$  be a dual spanning tree. Then there exists a unique solution  $(p, \theta)$  of the system of equations (A.1) and (A.2) such that  $(p, \theta)$  is feasible for (2.2).*

**Proof.** Let  $s = [\alpha, \beta]$ . Since  $(x, \alpha, \beta)$  is feasible for Equation (3.1),  $\sum_{i=1}^n s_i = 4\chi$ . Now, let  $p_f$  be the unique integer solution of Equation (A.3), guaranteed by Lemma A.0.2. Define the vector  $p \in \mathbb{Z}^l$ , such that  $p(e) = 0, \forall e \in \mathcal{T}$  and  $p(e) = p_f(e), \forall e \in \mathcal{E}^* \setminus \mathcal{T}$ . Then,  $p$  is the unique integer solution to Equation (A.1) that is also feasible for Equation (2.2). Let  $\omega = -r - \frac{\pi}{2}p - x$ , then  $\omega$  has a unique decomposition (up to two constants) as  $\omega = d_0 \omega_0 + d_1^T \omega_2 + B \omega_1$ . Since  $(x, \alpha, \beta)$  is feasible for TC, we have that  $\Gamma x = \frac{\pi}{2}s - s_g$ . Furthermore, we have that  $\frac{\pi}{2}s - s_g = -\Gamma r - \frac{\pi}{2}\Gamma p$ , due to Equation (A.1). Hence  $-\Gamma x - \Gamma r - \frac{\pi}{2}\Gamma p = \Gamma \omega = 0$ , and thus  $\omega$  is in the kernel of  $d_0^T$  and  $H^T$ . Since  $B^T = H^T - H^T d_0 (d_0^T d_0)^{\dagger} d_0^T$ , we have that  $\omega$  is also in the kernel of  $B$ , and thus  $\omega$  is orthogonal to the image of  $d_0$  and the image of  $B$ . Hence,  $\omega_0 = 0, \omega_1 = 0$ . Let  $c \in \mathcal{F}$  be the constrained face, and  $\theta_0$  the constrained value in Equation (2.2). Now,

set  $\theta = \omega_2 - (\omega_2(c) + \theta_0)\mathbb{1}$ , where  $\mathbb{1}$  is a constant vector with all ones. Then,  $\theta(c) = \theta_0$  and  $d_1^T\theta = d_1^T\omega_2 = \omega$ , because  $d_1^T\mathbb{1} = 0$ . Furthermore,  $\theta$  is defined uniquely, since  $\omega_2$  is unique up to a constant shift. Thus  $(p, \theta)$  is the unique solution of Equations (A.1), (A.2) that is also feasible for (2.2).

### Theorem A.1.

- (i) Let  $(\theta, p)$  be a feasible solution of (2.2). Then, for any integral basis of non-contractible dual cycles  $H$ , there exists a feasible solution  $(x, \alpha, \beta)$  of (3.1) such that  $E_T(x) = E_M(\theta, p)$ .
- (ii) Let  $(x, \alpha, \beta)$  be a feasible solution of (3.1). Then, for any dual spanning tree  $T$ , there exists a feasible solution  $(\theta, p)$  of (2.2) such that  $E_M(\theta, p) = E_T(x)$ .
- (iii) Let  $(x, \alpha, \beta)$  and  $(\theta, p)$  be corresponding solutions as in (i,ii), and let  $\theta_T$  be the integrated values of  $x$ . Then  $\theta_T = \theta \bmod \pi/2$ .

### Proof

- (i) Let  $(\theta, p)$  be a feasible solution of (2.2), and let  $(x, \alpha, \beta)$  be the feasible solution of Equation (3.1) guaranteed by Lemma A.0.3. Then  $-x = d_1^T\theta + r + \frac{\pi}{2}p$ , due to Equation (A.2). Thus  $E_M(\theta, p) = \|d_1^T\theta + r + \frac{\pi}{2}p\|_2^2 = \|-x\|_2^2 = E_T(x)$ .
- (ii) Let  $(x, \alpha, \beta)$  be a feasible solution of (3.1), and let  $(p, \theta)$  be the feasible solution of Equation (2.2) guaranteed by Lemma A.0.4. Then, Equation (A.1) again leads to  $E_M(\theta, p) = E_T(x)$ .
- (iii) Let  $(x, \alpha, \beta)$  and  $(\theta, p)$  be corresponding feasible solutions given by Equations (A.1), (A.2). Then,  $\theta_T$ , the integrated angle values, are computed by  $d_1^T\theta_T = -x - r$ . Furthermore, from Equation (A.2) we have that  $d_1^T\theta = -x - r - \frac{\pi}{2}p$ . Thus,  $d_1^T(\theta_T - \theta) = \frac{\pi}{2}p = 0 \bmod \frac{\pi}{2}$ . Since on the constrained face  $c \in \mathcal{F}$  we have that  $\theta_T(c) = \theta_c = \theta_0$ , we get that  $\theta_T - \theta = 0 \bmod \frac{\pi}{2}$ .

### Lemma A.0.5.

- (i) If  $(x, \alpha, \beta)$  is an optimal solution to Equation (3.1) then  $x = d_0a(\alpha) + Bb(\alpha, \beta)$ .
- (ii) If  $x = d_0a(\alpha) + Bb(\alpha, \beta)$  then  $E_T(x) = E_I(\alpha, \beta)$ .
- (iii) If  $(x, \alpha, \beta)$  is an optimal solution to Equation (3.1) then  $(\alpha, \beta)$  is a feasible solution to Equation (3.7).
- (iv) If  $(\alpha, \beta)$  is a feasible solution to Equation (3.7), then for  $x = d_0a(\alpha) + Bb(\alpha, \beta)$ , we have that  $(x, \alpha, \beta)$  is a feasible solution to Equation (3.1).

### Proof.

- (i) Let  $(x, \alpha, \beta)$  be an optimal solution of Equation (3.1). Then there exists a unique decomposition (up to two constants)  $x = d_0a + Bb + d_1^T c$ . Since  $x$  is optimal, the matrices  $d_0, B, d_1$  are mutually orthogonal and  $c$  is not constrained, then  $c = 0$ . Due to the constraints in (3.1) we have that  $d_0^T d_0 a = \frac{\pi}{2} \alpha - \alpha_g$ , thus  $a = a(\alpha) + c\mathbb{1}$  for some constant  $c \in \mathbb{R}$ . Hence,  $d_0 a = d_0 a(\alpha)$ , since  $\mathbb{1}$  is in the kernel of  $d_0$ . In addition, also due to the constraints in (3.1), we have  $H^T d_0 a + H^T B b = \frac{\pi}{2} \beta - \beta_g(\Gamma)$ , thus  $b = b(\alpha, \beta)$ .
- (ii) This is trivial, since  $d_0, B$  are orthogonal.
- (iii) This is trivial, since the constraints of (3.7) are a subset of the constraints of (3.1).
- (iv) Let  $(\alpha, \beta)$  be an optimal solution of Equation (3.7). Then  $\alpha^T \mathbb{1} = 4\chi$ , and  $(\frac{\pi}{2} \alpha - \alpha_g)^T \mathbb{1} = 0$ . Therefore, we have:  $d_0^T d_0 a(\alpha) = LL^\dagger (\frac{\pi}{2} \alpha - \alpha_g) = \frac{\pi}{2} \alpha - \alpha_g$ , since  $LL^\dagger m = m$  for any  $m$  orthogonal to the kernel of  $L$ . Furthermore,  $H^T d_0 a(\alpha) + H^T B b(\alpha, \beta) = H^T d_0 a(\alpha) + \frac{\pi}{2} \beta - \beta_g(\Gamma) - H^T d_0 a(\alpha) = \frac{\pi}{2} \beta - \beta_g(\Gamma)$ . Therefore, if we set  $x = d_0 a(\alpha) + B b(\alpha, \beta)$ , then  $(x, \alpha, \beta)$  fulfills the constraints in Equation (3.1).

**Theorem A.2.**  $(x, \alpha, \beta)$  is an optimal solution to Equation (3.1) if and only if  $x = d_0 a(\alpha) + B b(\alpha, \beta)$  and  $(\alpha, \beta)$  is an optimal solution to Equation (3.7).

### Proof.

- $\Rightarrow$  Let  $(x, \alpha, \beta)$  be an optimal solution of Equation (3.1). Then  $x = d_0 a(\alpha) + B b(\alpha, \beta)$  by Lemma A.0.5 (i). Assume that  $(\alpha, \beta)$  is not optimal for Equation (3.7). Then, there exists an optimal solution  $(\tilde{\alpha}, \tilde{\beta})$  such that  $E_I(\tilde{\alpha}, \tilde{\beta}) < E_I(\alpha, \beta)$ . But then, take  $\tilde{x} = d_0 a(\tilde{\alpha}) + B b(\tilde{\alpha}, \tilde{\beta})$ . According to Lemma A.0.5 we have that  $\tilde{x}$  is feasible, and  $E_T(\tilde{x}) = E_I(\tilde{\alpha}, \tilde{\beta}) < E_I(\alpha, \beta) = E_T(x)$ , contradicting the optimality of  $(x, \alpha, \beta)$ .
- $\Leftarrow$  Let  $(\alpha, \beta)$  be an optimal solution to Equation (3.7), and set  $x = d_0 a(\alpha) + B b(\alpha, \beta)$ , then according to Lemma A.0.5,  $(x, \alpha, \beta)$  is feasible for Equation (3.1). Assume that it is not optimal, then there exists an optimal solution  $(\tilde{x}, \tilde{\alpha}, \tilde{\beta})$  such that  $E_T(\tilde{x}, \tilde{\alpha}, \tilde{\beta}) < E_T(x, \alpha, \beta)$ . But since  $(\tilde{x}, \tilde{\alpha}, \tilde{\beta})$  is optimal, we have that  $\tilde{x} = d_0 a(\tilde{\alpha}) + B b(\tilde{\alpha}, \tilde{\beta})$ , and therefore  $E_T(\tilde{x}, \tilde{\alpha}, \tilde{\beta}) = E_I(\tilde{\alpha}, \tilde{\beta})$ . Hence, we have  $E_I(\tilde{\alpha}, \tilde{\beta}) = E_T(\tilde{x}, \tilde{\alpha}, \tilde{\beta}) < E_T(x, \alpha, \beta) = E_I(\alpha, \beta)$ , contradicting the optimality of  $(\alpha, \beta)$ .

## Appendix B

# Appendix - Supplementary Material.

We provide here the full quantitative results on the benchmark from Chapter 6.

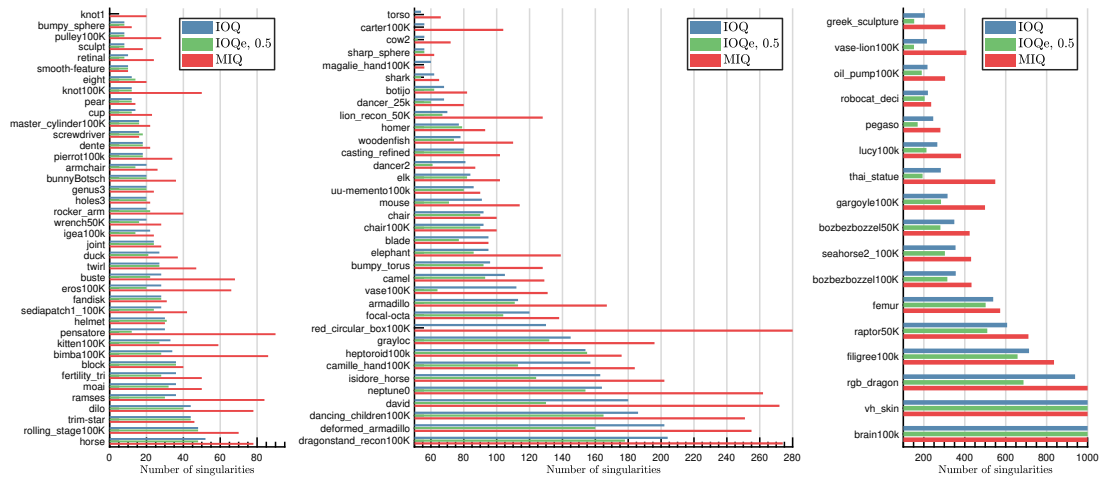


Figure B.1: Number of singularities.

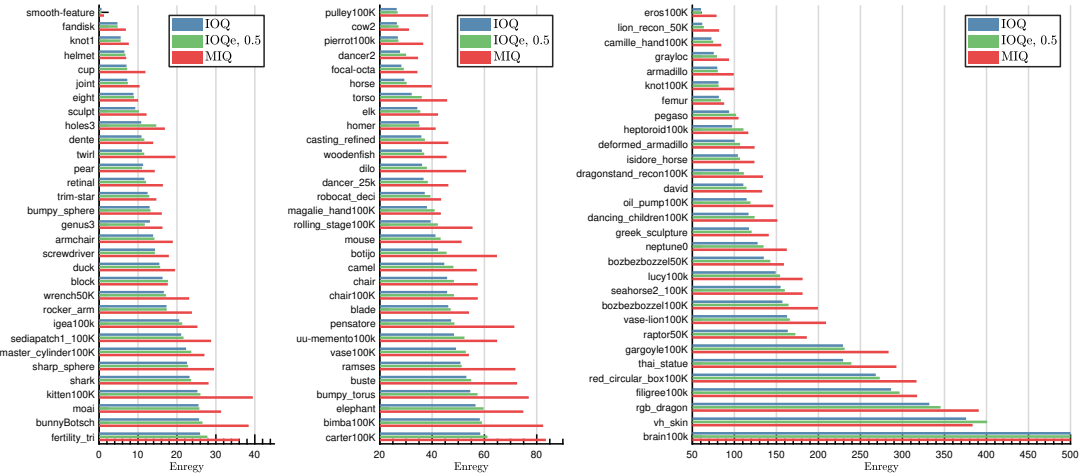


Figure B.2: Energy.

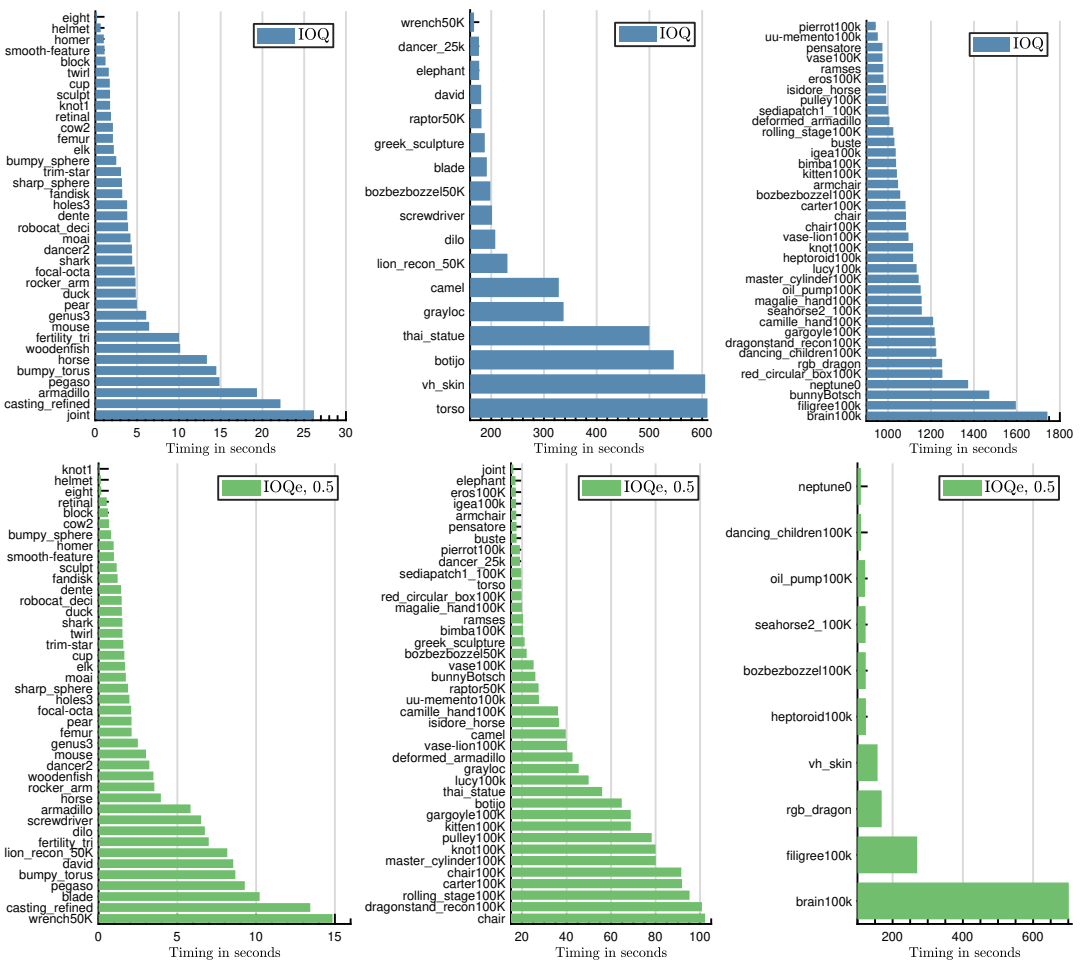


Figure B.3: Timing in seconds.

# Bibliography

- [Ach01] Dimitris Achlioptas. Database-friendly random projections. In *Proceedings of the twentieth ACM SIGMOD-SIGACT-SIGART symposium on Principles of database systems*, pages 274–281. ACM, 2001.
- [AEVZ02] Erik Agrell, Thomas Eriksson, Alexander Vardy, and Kenneth Zeger. Closest point search in lattices. *IEEE transactions on information theory*, 48(8):2201–2214, 2002.
- [BCGB08] Mirela Ben-Chen, Craig Gotsman, and Guy Bunin. Conformal flattening by curvature prescription and metric scaling. In *Computer Graphics Forum*, volume 27, pages 449–458. Wiley Online Library, 2008.
- [BCW17] Alon Bright, Edward Chien, and Ofir Weber. Harmonic global parametrization with rational holonomy. *ACM Transactions on Graphics (TOG)*, 36(4):89, 2017.
- [Bol13] Béla Bollobás. *Modern graph theory*, volume 184. Springer Science & Business Media, 2013.
- [BZK09] David Bommes, Henrik Zimmer, and Leif Kobbelt. Mixed-integer quadrangulation. *ACM Transactions On Graphics (TOG)*, 28(3):77, 2009.
- [CDGDS13] Keenan Crane, Fernando De Goes, Mathieu Desbrun, and Peter Schröder. Digital geometry processing with discrete exterior calculus. In *ACM SIGGRAPH 2013 Courses*, page 7. ACM, 2013.
- [CDS10] Keenan Crane, Mathieu Desbrun, and Peter Schröder. Trivial connections on discrete surfaces. In *Computer Graphics Forum*, volume 29, pages 1525–1533, 2010.
- [CRR<sup>+</sup>96] Ashok K Chandra, Prabhakar Raghavan, Walter L Ruzzo, Roman Smolensky, and Prasoon Tiwari. The electrical resistance of a graph

- captures its commute and cover times. *Computational Complexity*, 6(4):312–340, 1996.
- [CZ17a] Marcel Campen and Denis Zorin. On discrete conformal seamless similarity maps. *arXiv preprint arXiv:1705.02422*, 2017.
- [CZ17b] Marcel Campen and Denis Zorin. Similarity maps and field-guided t-splines: a perfect couple. *ACM Trans. Graph*, 36(4), 2017.
- [Dav13] Timothy A Davis. Algorithm 930: Factorize: An object-oriented linear system solver for matlab. *ACM Transactions on Mathematical Software (TOMS)*, 39(4):28, 2013.
- [DG03] Sanjoy Dasgupta and Anupam Gupta. An elementary proof of a theorem of johnson and lindenstrauss. *Random Structures & Algorithms*, 22(1):60–65, 2003.
- [DS84] Peter G Doyle and J Laurie Snell. *Random walks and electric networks*. Mathematical Association of America,, 1984.
- [DVPSH14] Olga Diamanti, Amir Vaxman, Daniele Panozzo, and Olga Sorkine-Hornung. Designing n-polyvector fields with complex polynomials. In *Computer Graphics Forum*, volume 33, pages 1–11. Wiley Online Library, 2014.
- [EBCK13] Hans-Christian Ebke, David Bommes, Marcel Campen, and Leif Kobbelt. QEx: robust quad mesh extraction. *ACM Transactions on Graphics (TOG)*, 32(6):168, 2013.
- [Epp03] David Eppstein. Dynamic generators of topologically embedded graphs. In *Proceedings of the fourteenth annual ACM-SIAM symposium on Discrete algorithms*, pages 599–608. Society for Industrial and Applied Mathematics, 2003.
- [JL84] William B Johnson and Joram Lindenstrauss. Extensions of lipschitz mappings into a hilbert space. *Contemporary mathematics*, 26(189-206):1, 1984.
- [JP<sup>+</sup>16] Alec Jacobson, Daniele Panozzo, et al. libigl: A simple C++ geometry processing library, 2016. <http://libigl.github.io/libigl/>.
- [JTPSH15] Wenzel Jakob, Marco Tarini, Daniele Panozzo, and Olga Sorkine-Hornung. Instant field-aligned meshes. *ACM Transactions on Graphics (TOG)*, 34(6):189, 2015.

- [KCPS13] Felix Knöppel, Keenan Crane, Ulrich Pinkall, and Peter Schröder. Globally optimal direction fields. *ACM Transactions on Graphics (TOG)*, 32(4):59, 2013.
- [Kir58] G Kirchhoff. On the solution of the equations obtained from the investigation of the linear distribution of galvanic currents. *IRE transactions on circuit theory*, 5(1):4–7, 1958.
- [LR07] Christian Liebchen and Romeo Rizzi. Classes of cycle bases. *Discrete Applied Mathematics*, 155(3):337–355, 2007.
- [MDSB03] Mark Meyer, Mathieu Desbrun, Peter Schröder, and Alan H Barr. Discrete differential-geometry operators for triangulated 2-manifolds. In *Visualization and mathematics III*, pages 35–57. Springer, 2003.
- [Mic01] Daniele Micciancio. The hardness of the closest vector problem with preprocessing. *IEEE Transactions on Information Theory*, 47(3):1212–1215, 2001.
- [MPZ14] Ashish Myles, Nico Pietroni, and Denis Zorin. Robust field-aligned global parametrization. *ACM Transactions on Graphics (TOG)*, 33(4):135, 2014.
- [MZ12] Ashish Myles and Denis Zorin. Global parametrization by incremental flattening. *ACM Transactions on Graphics (TOG)*, 31(4):109, 2012.
- [MZ13] Ashish Myles and Denis Zorin. Controlled-distortion constrained global parametrization. *ACM Transactions on Graphics (TOG)*, 32(4):105, 2013.
- [PS13] Giuseppe Patané and Michela Spagnuolo. An interactive analysis of harmonic and diffusion equations on discrete 3d shapes. *Computers & Graphics*, 37(5):526–538, 2013.
- [RLL<sup>+</sup>06] Nicolas Ray, Wan Chiu Li, Bruno Lévy, Alla Sheffer, and Pierre Alliez. Periodic global parameterization. *ACM Transactions on Graphics (TOG)*, 25(4):1460–1485, 2006.
- [RVLL08] Nicolas Ray, Bruno Vallet, Wan Chiu Li, and Bruno Lévy. N-symmetry direction field design. *ACM Transactions on Graphics (TOG)*, 27(2):10, 2008.
- [SG17] Saeid Sahraei and Michael Gastpar. Polynomially solvable instances of the shortest and closest vector problems with applications to compute-and-forward. *IEEE Transactions on Information Theory*, 63(12):7780–7792, 2017.

- [SSP08] Boris Springborn, Peter Schröder, and Ulrich Pinkall. Conformal equivalence of triangle meshes. In *ACM Transactions on Graphics (TOG)*, volume 27, page 77. ACM, 2008.
- [ST04] Daniel A Spielman and Shang-Hua Teng. Nearly-linear time algorithms for graph partitioning, graph sparsification, and solving linear systems. In *Proceedings of the thirty-sixth annual ACM symposium on Theory of computing*, pages 81–90. ACM, 2004.
- [ST14] Daniel A Spielman and Shang-Hua Teng. Nearly linear time algorithms for preconditioning and solving symmetric, diagonally dominant linear systems. *SIAM Journal on Matrix Analysis and Applications*, 35(3):835–885, 2014.
- [TLHD03] Yiying Tong, Santiago Lombeyda, Anil N Hirani, and Mathieu Desbrun. Discrete multiscale vector field decomposition. In *ACM transactions on graphics (TOG)*, volume 22, pages 445–452. ACM, 2003.
- [VCD<sup>+</sup>16] Amir Vaxman, Marcel Campen, Olga Diamanti, Daniele Panozzo, David Bommes, Klaus Hildebrandt, and Mirela Ben-Chen. Directional Field Synthesis, Design, and Processing. *Computer Graphics Forum*, 2016.





נמצא באופן אקראי, אזי בהסתברות גבוהה המרחק האוקלידי בין הנקודות לא ישנה יתר על המידה. מכיוון שהיחס מטריצה ההטנדויות שקול לחישוב מרחקים אוקלידיים, ניתן לקבל קירוב של המטריצה על ידי שימוש בהורדת מימד מסווג זה, ובהסתברות גבוהה הקירוב יהיה מוצלח. יתרון נוסף של גישה זו הוא שגם את חישוב המרחקים האוקלידיים במימד הנמצא ניתן לחשב באופן מקביל על מעבד גרפי, דבר המאפשר שיפור ניכר בביטויים מבחינה מעשית.

בתזה זו אנו מציגים את שיטתנו תוך שימוש בקירוב וכן באמצעות חישוב מדויק של המטריצה, ומודגמים כי בשני המקרים אנו מקבלים תוצאות טובות יותר מאשר קודמות לפיה מدد חלקות ומספר נקודות הסינגולריות. כמו כן, אנו מראים באופן אינטuitיבי וכמוותי שהשיטה מתכנסת לפתרון מיטבי גם כאשר משתמשים בקירוב, שהינו אקראי בסיסו. לבסוף, אנו מוכחים את השקילות בין שתי הגישות המתוארכות.

## תקציר

שדות וקטורים כיווניים הם אובייקטים בעלי חשיבות רבה בעיבוד גיאומטריה ספרטית עם מגוון של יישומים כגון סינטזה של מרקמים, רינדור מסונן, מעבר מבוסות דיסקרטי מושלשי למשתוח דיסקרטי ריבועי, ותכנו אדריכלי. למשל, אחת הגישות למעבר מבוסות דיסקרטי מושלשי למשתוח דיסקרטי ריבועי היא על ידי חישוב פרמטריזציה, כלומר, מיפוי מהמשתוח  $L^2$  [2], תוך הדרישה שאורינטיציות הפרמטריזציה תהיה מושרת עם כיווני השדה. כדוגמה נספחת, ניתן להשתמש בכיוונים של השדה בצד להגדיר "כיוון מכחול" כאשר רוצים לрендר באופן מסונן את המשטח.

עובדת זו מתמקדת בשדות וקטורים מצטלבים – שדות כיווניים בהם בכל נקודה על המשטח מוגדרים ארבעה וקטורי ייחידה עם סימטריה של  $2/\pi$ . חישוב שדות וקטורים מצטלבים הינה בעיה מורכבת, שכן ניסוח הבעיה תלוי במשתנים שלמים אשר משמשים לייצוג האינווריאנטיות לסיבוב בכפולות של  $2/\pi$ . כמו כן, מציאת המיקום האופטימלי עבור נקודות הסינגולריות היא בהמותה בעיה קומבינטורית קשה.

בתזה זו אנו מציגים אלגוריתם איטרטיבי חדש לחישוב שדות וקטורים מצטלבים על פני משטח דיסקרטי מושלשי. האלגוריתם פשוט, ניתן לחישוב באופן מקבילי על מעבד גרפי, ומוצא פתרונות עם אנרגיה נמוכה יותר ופחות נקודות סינגולריות מאשר שיטות קודמות. בנוסף, מובטח כי לא ניתן למצוא מתחם חדש נקודות סינגולריות אחת של  $2/\pi \pm$  באופן שיקטין את האנרגיה.

הגישה שלנו מבוססת על שיקולות פורמלית, אותה אנו מוכחים, בין שני ניסוחים שונים של הבעיה. בגישה הראשונה, השדה מיוצג על ידי זווית עברו כל פאה, המייחסת למערכת צירים שרירותית במישור של אותה פאה, והפתרון הוא השדה שלו ארגנטית דרייליה המינימאלית, כאשר יש להתחשב בסימטריה של  $2/\pi$ . בגישה השנייה השדה מיוצג בתווך השינוי בזווית מעבר מפהה לפאה שכנה. בכך, נוצר אוסף של אילוצים הנובעים ממסלולים מעגליים על פני המשטח, והמשתנים השלמים עוברים לאלוצים במקומות להיות חלק מפונקציית המטריה.

שיקולות זו מאפשרת לנו להסיר את המשתנים המשמשים מניסוח הבעיה ולפתח שיטת חישוב יעילה עבור נקודות הסינגולריות. הניסוח שלנו משתמש במטריצה מותורת הגרפים הנקרואת מטריצת ההתנגדויות של הגרף. מקור מטריצה זו בטורת החסמל, שם ערכה עברו קשת של הגרף שווה להפרש הפוטנציאלים המתפתח בין קצויות הקשת כאשר אורמת דרכה יחידת זרם אחת. ניתן גם לחישוב על ערך זה בעל משך הנסעה בין שני קדוקדים על הגרף, או בעל הסתברות שקשת תופיע בעץ פורש של הגרף הנבחר באקראי. כדי להאיץ את החישוב ולאפשר تعدודו של קיצור זמן החישוב על פני חלוקות התוצאה, אנו משתמשים בשיטה מוכרת לקירוב מטריצת ההתנגדויות של הגרף הבוסט על הטלה אקראית. שיטה זו משתמשת על מנת ג'ונסון-לינדנשטיראוס, לפיה כאשר מטילים אוסף נקודות ממוחב אוקלידי על מימד גבוה למימד



המחקר בוצע בהנחייתה של פרופסור מירלה בר-חן, בפקולטה למדעי המחשב.

חלק מן התוצאות בחיבור זה פורסמו כמאמרים מאת המחבר ושותפיו למחקר בכנסים ובכתבי-עת במהלך תקופה מהימן של המחבר, אשר גרסאותיהם העדכניות ביוטר הינן:

Nahum Farchi and Mirela Ben-Chen. Integer-only cross field computation. *ACM Transactions on Graphics (TOG)*, 37(4), 2018.

## תודות

ברצוני להודות למירלה שהנחתה אוטי במקצועיות וסבלנות רבה בעת כתיבת התזה. כמו כן, אני מודה למשפחתי ולחברי על התמיכה והעידוד לאורך הדרכן.

אני מודה לטכניון על התמיכה הכספית הנדיבה בהשתלמותי.



# **תכnuן שדות מצטלבים במספריים שלמים**

**חיבור על מחקר**

לשם מילוי חלקו של הדרישות לקבלת התואר  
**מגיסטר למדעים במדעי המחשב**

**נחות פרחי**

הוגש לסנט הטכניון --- מכון טכנולוגי לישראל  
סיוון התשע"ח      חיפה      מאי 2018



# **תכנו שדות מצלבים במספרים שלמים**

**נחות פרחי**